

Multi-Wavelength Monitoring and Reverberation Mapping of a Changing Look Event in the Seyfert Galaxy NGC 3516

V. L. Oknyansky,^{1*} M. S. Brotherton,² S. S. Tsygankov,^{3,4} A. V. Dodin,¹ D. -W. Bao,⁵ B. -X. Zhao,⁶ P. Du,⁵ M. A. Burlak,¹ N. P. Ikonnikova,¹ A. M. Tatarnikov,¹ A. A. Belinski,¹ A. A. Fedoteva,¹ N. I. Shatsky,¹ E. O. Mishin,¹ S. G. Zheltouhov,¹ S. A. Potanin,^{1,7} J. -M. Wang,^{5,8} J. N. McLane,² H. A. Kobulnicky,² D. A. Dale,² T. E. Zastrocky,^{2,9} J. Maithil,² K. A. Olson,² C. Adelman,^{2,10} Z. Carter,^{2,11} A. M. Murphree,^{2,12} M. Oeur,^{2,13} S. Schonsberg,^{2,14} T. Roth^{2,15}

¹Sternberg Astronomical Institute, M.V. Lomonosov Moscow State University, 119234, Moscow, Universitetsky pr-t, 13, Russia

²Department of Physics and Astronomy, University of Wyoming, Laramie, WY 82071, USA

³Department of Physics and Astronomy, FI-20014 University of Turku, Turku, Finland

⁴Space Research Institute of the Russian Academy of Sciences, Profsoyuznaya Str. 84/32, Moscow 117997, Russia

⁵Key Laboratory for Particle Astrophysics, Institute of High Energy Physics, Chinese Academy of Sciences, 19B Yuquan Road, Beijing 100049, China

⁶Shanghai Astronomical Observatory, Chinese Academy of Sciences, Shanghai 200030 China

⁷Faculty of Physics, Moscow M.V. Lomonosov State University, Leninskie gory 1, Moscow, 119991, Russia

⁸School of Astronomy and Space Science, University of Chinese Academy of Sciences, 19A Yuquan Road, Beijing 100049, China

⁹Physics and Astronomy Department, Regis University, Denver, CO 80212, USA

¹⁰Department of Physics & Astronomy, Poly Pomona, Pomona, CA 91768, USA

¹¹Department of Physics and Astronomy, Trinity University, San Antonio, TX 78212, USA

¹²Department of Physics, Rhodes College, Memphis, TN 38112, USA

¹³Department of Physics and Astronomy, State Long Beach, Long Beach, CA 90840, USA

¹⁴Department of Physics and Astronomy, University of Montana, Missoula, MT 59812, USA

¹⁵Department of Physics & Astronomy, California State University, Sacramento, CA 95747, USA

Received ... Accepted ...

ABSTRACT

We present the results of photometric and spectroscopic monitoring campaigns of the changing look AGN NGC 3516 carried out in 2018 to 2020 covering the wavelength range from the X-ray to the optical. The facilities included the telescopes of the CMO SAI MSU, the 2.3-m WIRO telescope, and the XRT and UVOT of *Swift*. We found that NGC 3516 brightened to a high state and could be classified as Sy1.5 during the late spring of 2020. We have measured time delays in the responses of the Balmer and He II $\lambda 4686$ lines to continuum variations. In the case of the best-characterized broad H β line, the delay to continuum variability is about 17 days in the blue wing and is clearly shorter, 9 days, in the red, which is suggestive of inflow. As the broad lines strengthened, the blue side came to dominate the Balmer lines, resulting in very asymmetric profiles with blueshifted peaks during this high state. During the outburst the X-ray flux reached its maximum on 1 April 2020 and it was the highest value ever observed for NGC 3516 by the *Swift* observatory. The X-ray hard photon index became softer, ~ 1.8 in the maximum on 21 Apr 2020 compared to the mean ~ 0.7 during earlier epochs before 2020. We have found that the UV and optical variations correlated well (with a small time delay of 1–2 days) with the X-ray until the beginning of April 2020, but later, until the end of Jun. 2020, these variations were not correlated. We suggest that this fact may be a consequence of partial obscuration by Compton-thick clouds crossing the line of sight.

Key words: galaxies: Seyfert; galaxies: nuclei; galaxies: individual: NGC 3516; galaxies: photometry; (galaxies:) quasars: emission lines; X-rays: galaxies

1 INTRODUCTION

The spectral variability of NGC 3516 was first discovered by [An-drillat & Souffrin \(1968\)](#) when they compared their 1967 spec-

* E-mail: oknyan@mail.ru

trum and spectrophotometric results (for 1965–1966) from [Dibai & Pronik \(1968\)](#) with earlier data from [Seyfert \(1943\)](#). That was not only the first detection of spectral variability for Seyfert galaxies but also the first example of an Active Galactic Nucleus (AGN) changing its spectral type - a Changing-Look (CL) AGN. That happened a bit earlier than the continuum variations in the Seyfert galaxy NGC 4151 were reported by [Fitch et al. \(1967\)](#) and, therefore, [Andrillat & Souffrin \(1968\)](#) suspected the forbidden lines to have changed dramatically, and the continuum and Balmer lines not to be short-term variable, although the reverse is accepted as true today. The discovery of the H α variability for NGC 3516 and, at the same time, the first reverberation mapping (RM) for line variations relative to the continuum (for AGN in general) was done in 1973 by [Cherepashchuk & Lyutyi \(1973\)](#). To date, the CL events were found in tens of AGNs including QSOs (see e.g., [MacLeod et al. 2016](#); [Runco et al. 2016](#)). A detailed study of a CL AGN can be very useful for the understanding of the physics and evolution of AGNs.

NGC 3516 was investigated very intensively during the past half century. The studies included high-cadence optical photometry ([Lyutyi & Doroshenko 1993](#)), spectral monitoring ([Wanders et al. 1993](#); [Fausnaugh et al. 2016](#); [Shapovalova et al. 2019](#)), X-ray observations ([Noda et al. 2016](#); [Buisson et al. 2017](#)) and IR photometry ([Koshida et al. 2014](#)). The first RM (with the use of some statistical analysis) for NGC 3516 was done by [Wanders et al. \(1993\)](#) who found time delays of about 15 and 7 days between the H α and H β variations and the continuum changes, respectively.

The velocity-resolved RM program conducted in 2007 ([Denney et al. 2009](#)) for the H β emission line demonstrated that the highest positive velocities exhibited the shortest lags, with the lags steadily growing toward negative velocities. The situation appears to have changed to the opposite in 2012 ([De Rosa et al. 2018](#)). The delay for different velocity bins in the emissionline profile varied from a few days to 18 days. This behaviour could be interpreted as a signature of infalling gas motion in 2007 and outflowing in 2012, respectively. The RM relative to X-ray and UV variations yielded controversial results. The first conclusion that the delay between the X-ray flux variations and those of the optical is about 100–200 days ([Maoz et al. 2002](#)) was not subsequently confirmed by later studies, whereas a delay of 2 days between X-ray and UV variability seemed more likely ([Noda et al. 2016](#); [Buisson et al. 2017](#)).

During the last 8 years NGC 3516 was in a very low state with some re-brightening at the end of 2015 and the first half of 2016. In 2014 a CL event was detected when the broad H β was quite faint ([Shapovalova et al. 2019](#)) and an additional CL event was observed in 2016 when broad emission lines were in the high state again ([Oknyansky et al. 2020a](#)). From the second half of 2016 till the end of 2018 the object was in the low state with broad emission lines being very weak. In our previous study ([Ilić et al. \(2020\) = Paper I](#)) we reported on the awakening of the object after several years of being in a very low state. We found a brightening of the continuum with a maximum at the end of Nov. 2019. At the beginning of Dec. 2019 the broad double-peaked components of H β and H α were detected and they were more prominent than in 2018 ([Shapovalova et al. 2019](#)). Also strong high-ionisation coronal lines like [Fe x] λ 6374 were present in the spectra and suspected to be variable. Preliminary results of our research on the flare and new CL event in NGC3516 were mentioned by [Oknyansky et al. \(2020c\)](#). Here we present a continuation of our research based on newer and more extensive data for NGC 3516. Such consistently variable objects as NGC 3516 straddling the line between different classes represent special laboratories to study CL events.

Table 1. Results of optical photometry with the RC600 CMO in *UB* bands. (Note: The full version of this table is available in its entirety in machine-readable form.)

J.D.-2450000	mag	Band
8746.54	14.249 \pm 0.010	<i>B</i>
8746.54	14.380 \pm 0.006	<i>U</i>
8749.53	14.401 \pm 0.006	<i>U</i>
8749.55	14.269 \pm 0.004	<i>B</i>
8766.55	14.309 \pm 0.010	<i>U</i>
...

2 OBSERVATIONS, INSTRUMENTS AND DATA REDUCTION

We started photometric (*UBVR*cl**) monitoring of NGC 3516 in September 2019 in order to check if the object was in the low state as reported by [Shapovalova et al. \(2019\)](#). As soon as we detected a brightening at the end of November 2019 we started spectral observations (from 7 December 2019) with the 2.5-m telescope of the Caucasian Mountain Observatory (CMO) of the Sternberg Astronomical Institute (SAI) of Moscow State University (MSU). Preliminary results of the research were published in Paper I. Here we present the next part of the study based on intensive photometric and spectral observations from December 2019 to July 2020. We also report new *Swift* X-ray, UV/optical data obtained in Feb.–Jun. 2020. The data are complemented by high-cadence spectroscopy obtained with the 2.3-m Wyoming Infrared Observatory (WIRO) telescope in 2018–2020. The details of the observations and data reduction as well as relevant references are given in the next subsections, whereas the results are presented and discussed in the following section.

2.1 Optical photometry

We obtained optical *UBVR*cl** CCD data with RC600, a new 60-cm automated telescope located at the CMO, for nearly 10 months since September 2019 (a total of 126 nights, with a cadence of about 2 days). The telescope, photometer, and the photometry methods were described by [Berdnikov et al. \(2020\)](#) and also in Paper I. Comparison stars from [Lyutyi & Doroshenko \(1993\)](#) were used. During this more than 9 month period, the data were obtained mostly under photometric conditions, several exposures (2–6) were made for each band, with typical exposure times varying from 300–360 s for the *U* band to 20–30 s for *B*. We used an aperture of 6.7 arcsec (diameter). The consistency of the individual multiple magnitudes measured each night, usually three, was usually not worse than 0.01 mag, however the error could be few times bigger in case of bad conditions or during bright Moon light contamination. The *UB* light curves are presented in Fig. 1–2 and Table 1. In Fig. 1 we also show the already published optical *B* photometry since 1999 (see [Shapovalova et al. \(2019\)](#) and Paper I for details).

2.2 *Swift* Optical, Ultraviolet, and X-ray observations

The *Neil Gehrels Swift Observatory* ([Gehrels et al. 2004](#)) observed NGC 3516 in 2006 but only since 2012 it started semi-regular monitoring. Some of these data (obtained in 2006–2017) were published in [Buisson et al. \(2017\)](#) and Paper I. In addition to the data

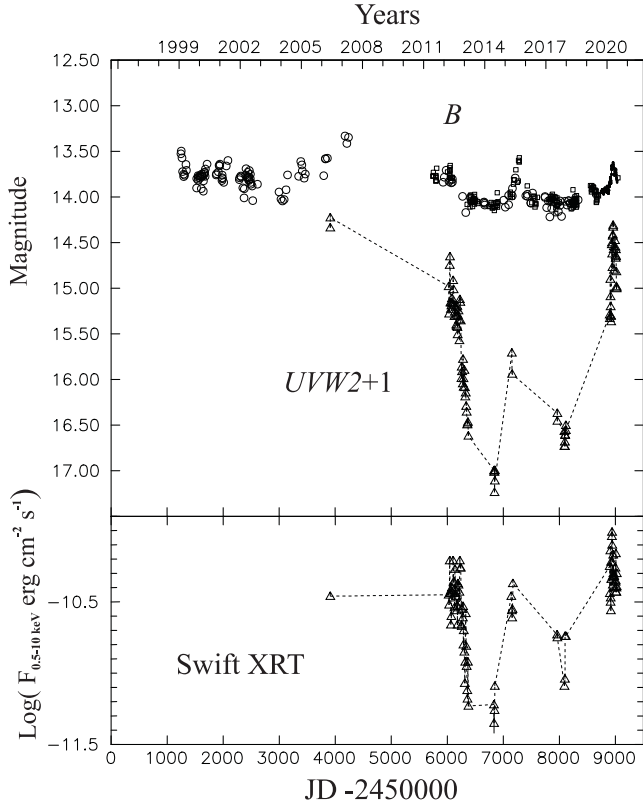


Figure 1. Multi-wavelength observations of NGC 3516 in 1999–2020. *Top Panel:* Light curves in the *B* and *UVW2* bands for an aperture of 10 arcsec. The large open circles denote data from Shapovalova et al. (2019), the open boxes stand for the data from the SAI Crimea campaign and are shown for continuity (see Lyutyi & Doroshenko (1993) and Paper I for details). The points represent the estimates (nightly means) obtained with RC600 (partly presented in Paper I). The open triangles are the *UVW2* data obtained with *Swift*/UVOT. *Bottom Panel:* The *Swift*/XRT 0.5–10 keV X-ray flux (in $\text{erg cm}^{-2} \text{s}^{-1}$).

available in the archive, we applied for a new TOO program starting from 19 Feb 2020 and continuing until the end of June 2020 (a total of 32 new dates), with a cadence of 3 days (however some of the scheduled observations were not executed and so the real mean sampling was just about 4 days). All the data were reduced uniformly with the most recent versions of the software and calibration files.

The *Swift* Ultraviolet/Optical Telescope (UVOT) observes the source in different filters (*V*, *B*, *U*, *UVW1*, *UVW2*, *UVM2*) simultaneously with the XRT telescope. The image analysis has been done following the procedure described on the web-page of the UK Swift Science Data Centre. Photometry was performed using the procedure `UVOTSOURCE` from the `heasoft` package. The source and background apertures were chosen with radii of 5 and 10 arcsec, respectively.

The XRT telescope (Burrows et al. 2005) observed NGC 3516 in photon counting (PC) and windowed timing (WT) modes, depending on target brightness. All the new observations were made only in PC mode. The spectrum obtained in each observation was prepared using the online tools provided by the UK Swift Science Data Centre (http://www.swift.ac.uk/user_objects/; Evans et al. 2009). The method used was the same as described in Oknyansky et al. (2017, 2019b) and Paper I. The light curves in X-

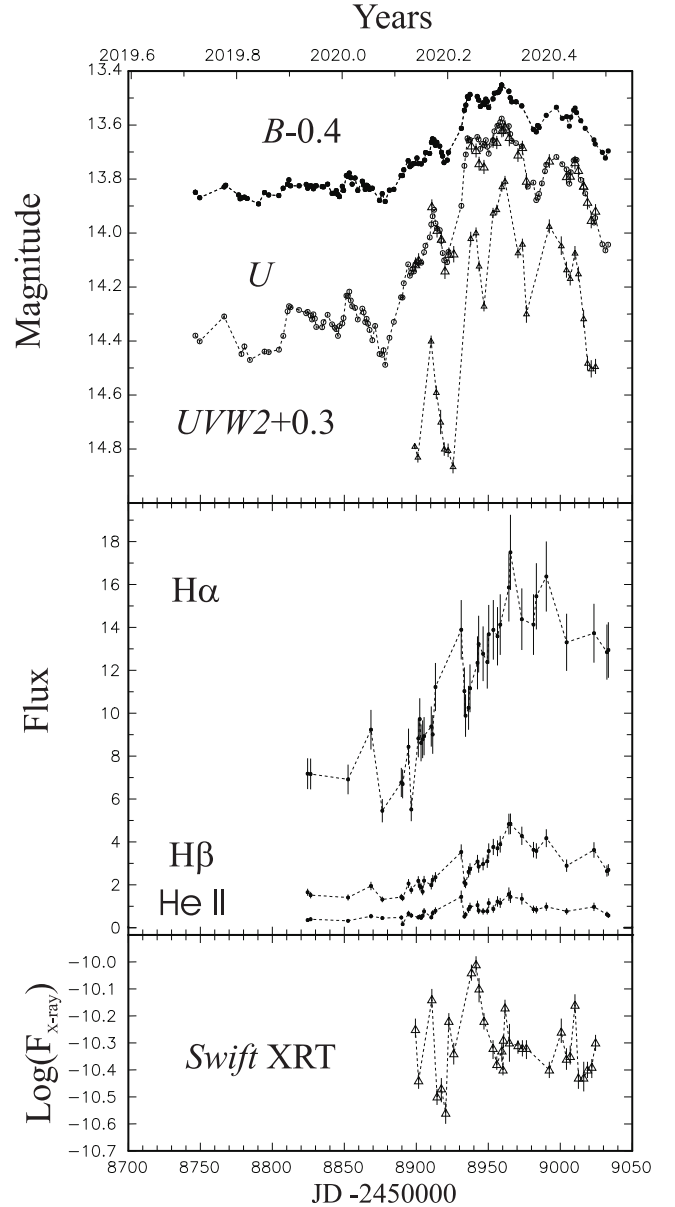


Figure 2. Multi-wavelength observations of NGC 3516 shown for 2019–2020 only. *Top Panel:* Light curves in *BU* (an aperture of 6.7 arcsec) and *UVW2* (an aperture of 10 arcsec). The nightly mean *B* (filled circles) and *U* (open circles) estimates obtained with RC600. The *U* data obtained with *Swift*/UVOT and reduced to the same system and aperture as the RC600 data (triangles). *Middle Panel:* Variations of the fluxes (in units $10^{-13} \text{ erg s}^{-1} \text{ cm}^{-2}$) of $\text{H}\alpha$, $\text{H}\beta$ and He II from the spectral data obtained with the 2.5-m telescope of CMO SAI MSU (see text). *Bottom Panel:* The *Swift*/XRT 0.5–10 keV X-ray flux (in $\text{erg cm}^{-2} \text{s}^{-1}$) – (triangles).

ray *Swift*/XRT) and ultraviolet (*Swift*/UVOT/*UVW2*) are presented in Fig. 1 (2006–2020) and Fig. 2 (2020). The *U* data obtained with *Swift*/UVOT presented in Fig. 2 are reduced to the same system and aperture as the RC600 data using a linear least squares regression. Obtained data give us opportunities to trace the source evolution on long and short timescales.

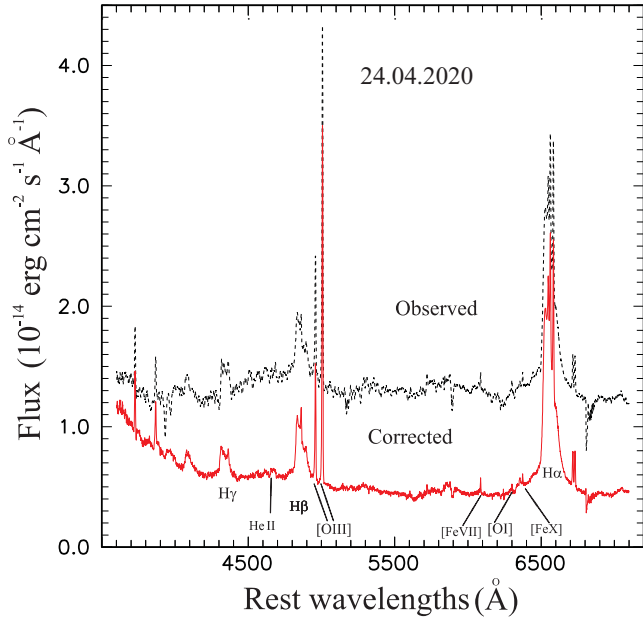


Figure 3. The isolated nuclear non-stellar spectrum (solid line) of NGC 3516 for 24.04.2020 obtained by subtracting the host galaxy spectrum from the observed (dashed line). See text for details.

2.3 Spectral observations at CMO SAI MSU

We obtained optical spectra (range 3500–7000 Å) using the 2.5-m telescope of the Caucasian Mountain observatory (CMO) of SAI MSU (further CMO, see Paper I for details) during 40 nights from 7 Dec. 2019 to 4 Jul. 2020 with a cadence of about 5 days. The telescope is equipped with the medium resolution optical Transient Double-beam Spectrograph (TDS), with Andor Newton 940P cameras using CCDs E2V CCD42-10, and a volume phase holographic grating (Potanin et al. 2020). The slit width in most cases was 1′.0, and 1′.5 for 9 Dec. 2019. The exposure times were from 1200 s to 3600 s, giving a spectral resolution and S/N ratio of ~ 4 Å and 50–120 near H β , and ~ 3 Å and 70–140 near H α . Standard data reduction procedures were performed using self-developed Python3 scripts (see Paper I for details). The spectrum of the nuclear region representing the flux collected within an aperture of 6 arcsec centered on the nucleus was flux-calibrated using spectrophotometric standard stars. We corrected the spectra for the host galaxy contamination which was estimated by scaling the off-nucleus spectrum measured between 6 and 16 arcsec on both sides from the centre of the nucleus. The narrow emission lines of NGC 3516 extend more than 20 arcsec from the nucleus and are clearly seen in our spectra (see e.g., Wanders et al. 1993). We linearly interpolated under these extended narrow lines to remove them from the host galaxy spectrum. The resulting host galaxy spectrum was then scaled by a factor that was adjusted until the stellar absorption features matched those in the object spectrum. To scale H β we used an assumption that the [O III] $\lambda 5007$ line was not variable during the months of our monitoring. For extended sources (as in the case of NGC 3516) this method might be not quite suitable and it is needed to correct the data some way for seeing effects (e.g., Wanders et al. 1993; Feng et al. 2021b). Additionally (as a part of our standard calibration procedure), we corrected the data for seeing effects using our optical photometry, which was obtained on the same dates as the spectra. We assumed that the optical continuum flux variability

Table 2. Spectral lines and the wavelength ranges (in Å) for integrating the line intensities.

Spectral line	wavelengths (CMO)	wavelengths (WIRO)
H α	6380 – 6700	6480 – 6670
H β	4757 – 4936	4760 – 4930
H β (Blue)	4815 – 4853	4800 – 4845
H β (Red)	4876 – 4936	4880 – 4930
H γ	4260 – 4406	–
He II	4544 – 4695	–

at different wavelengths is synchronous with a linear dependence between those wavelengths. This assumption is supported by our cross-correlation and RM investigations for the variability in the *U* and *B* filters (see further Sec. 3.3 and Table 1). We used the *U* band photometry to correct our spectra since in this band the amplitude variation is a few times larger than in the *B* and *V* bands but the accuracy is about the same for these bands. We estimate the accuracy of such the calibration of the host-corrected spectra to be $\sim 1\%$. So, the errors of the emission-line intensities are mostly dependent upon the continuum level fitting errors. As an example, Fig. 3 shows the full spectrum for 24 Apr. 2020 (both observed and corrected for the host galaxy input). Fig. 4 shows some spectra (corrected for the host galaxy) for selected dates during January – June 2020. Dramatic variations of the broad lines and of the UV continuum are visible. Fig. 5 shows the mean and root-mean-square (rms) spectra in the H β region for CMO data (for details see Du et al. (2018)). We note that the variation of seeing and small errors in wavelength calibration will affect the shapes of narrow lines (Peterson 2004; Feng et al. 2021b). Meanwhile, the [O III] (as well as other forbidden lines) and the narrow H β emission lines which are seen in the rms spectra are very small relative to these lines in the mean spectrum and that is an indication of reasonable calibration procedure. As seen from the rms spectra, the variability in broad H β as well as in H α and H γ lines was significant and asymmetric.

In Fig. 2 we present the variations of the broad H α and H β flux (here and further, see the wavelength ranges for integrating the line intensities in Table 2) relative to the [O III] $\lambda 5007$ flux. The same ratios were calculated for the blue wing of H β – $I(\text{H}\beta(\text{Blue}))$ and for the red wing of H β – $I(\text{H}\beta(\text{Red}))$. Previous to integration, we removed the narrow components with zero velocity in H α and H β , by fitting them with a Gaussian plus a linear background. The latter may represent some contribution of underlying broad components, which can be nearly linear over a small wavelength range. Similarly, the [N II] $\lambda 6548, \lambda 6584$ narrow lines were removed from H α . We also integrated fluxes of H γ (blended with [O III] $\lambda 4363$) and He II $\lambda 4686$ (blended with Fe II) relative to [O III] $\lambda 5007$ without removing narrow components (further, for brevity, H γ and He II, respectively). The variations of He II are shown in Fig. 2. We present all these values and associated errors in Table 3. The errors were estimated from the internal consistency of the data for close dates. Fig. 6 shows spectra for the H β region for dates of minimum and maximum flux (10 Feb. 2020 and 24 Apr. 2020), as well as the difference spectrum, and the regions of integration for $I(\text{H}\beta)$, $I(\text{H}\beta(\text{Blue}))$ and $I(\text{H}\beta(\text{Red}))$.

2.4 Spectral observations at WIRO

A significant part of our spectral data set was obtained with the 2.3 meter Wyoming Infrared Observatory (WIRO) telescope from Nov.

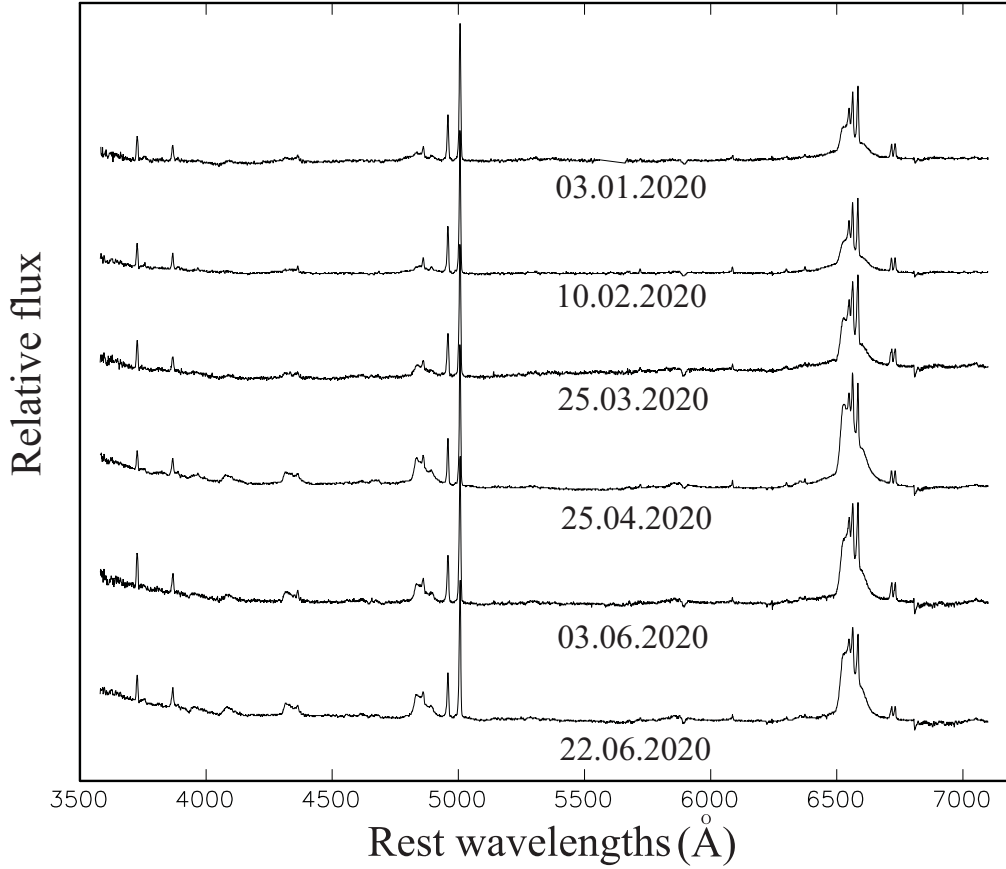


Figure 4. The selected host-galaxy subtracted spectra, obtained in the CMO for those spectra covering the total wavelength range. All spectra are normalized to the [O III] $\lambda 5007$ intensity and shifted for comparison.

Table 3. Results of optical spectroscopy with the 2.5-m telescope at CMO. (Note: The full version of this table is available in its entirety in machine-readable form.)

J.D.-2450000	H α *	H β *	H β (blue)*	H β (red)*	H γ *	He II*
8824.57	3.26 \pm 0.33	0.75 \pm 0.08	0.24 \pm 0.02	0.22 \pm 0.02	0.40 \pm 0.05	0.16 \pm 0.03
8826.59	3.26 \pm 0.33	0.69 \pm 0.07	0.23 \pm 0.02	0.22 \pm 0.02	0.39 \pm 0.05	0.18 \pm 0.04
8852.59	3.14 \pm 0.31	0.64 \pm 0.06	0.23 \pm 0.02	0.16 \pm 0.02	0.35 \pm 0.05	0.15 \pm 0.03
8868.57	4.20 \pm 0.42	0.89 \pm 0.09	0.34 \pm 0.03	0.20 \pm 0.02	0.62 \pm 0.08	0.24 \pm 0.05
8876.40	2.48 \pm 0.25	0.60 \pm 0.06	0.22 \pm 0.02	0.15 \pm 0.02	0.36 \pm 0.05	0.20 \pm 0.04
...

* Flux value relative to [O III] $\lambda 5007$ which mean-weighted flux is 2.2×10^{-13} erg cm $^{-2}$ s $^{-1}$.

2018 until 31 May 2020 with a cadence of about 4 days but which includes a seasonal gap. The observation and reduction methods were the same as described by Du et al. (2018). The primary differences compared to the CMO spectral data consist of a wider aperture (5 arcsec oriented north-south) and correspondingly lower spectral resolution (~ 10 Å for a uniformly filled slit). Typically we observed NGC 3516 in three 300 second exposures and flux calibrated the spectra using spectrophotometric standards G191B2B, Feige 34, HZ 44, or BD+28°4211. We corrected the spectra for the host galaxy contamination in the same way as it was described before for the CMO spectral data. Fig. 7 shows some spectra (corrected for the host galaxy) for selected dates during January – June 2020. Dramatic brightenings of the broad H β line occurred twice. The mean and root-mean-square (rms) spectra in H β region (just

WIRO data) for NGC 3516 are shown in Fig. 8 (for details see Du et al. (2018)). The [O III] and the narrow H β emission lines in the rms spectra are not seen, since there is no variability and that is an indication of correct calibration procedure. As it is seen from the rms spectra the variability in the broad H β and H α lines was significant and asymmetric.

The spectral data obtained at WIRO and CMO were processed completely independently, and therefore, as well as due to different spectral resolutions, the spectral intervals for integration within the broad H β line were set slightly differently. The H α and H β fluxes see Table 2 normalized to the O [III] $\lambda 5007$ flux. The same ratios but only for the blue H β (Blue) and red H β (Red) wings of the line were calculated.. Narrow emission-lines were removed before the

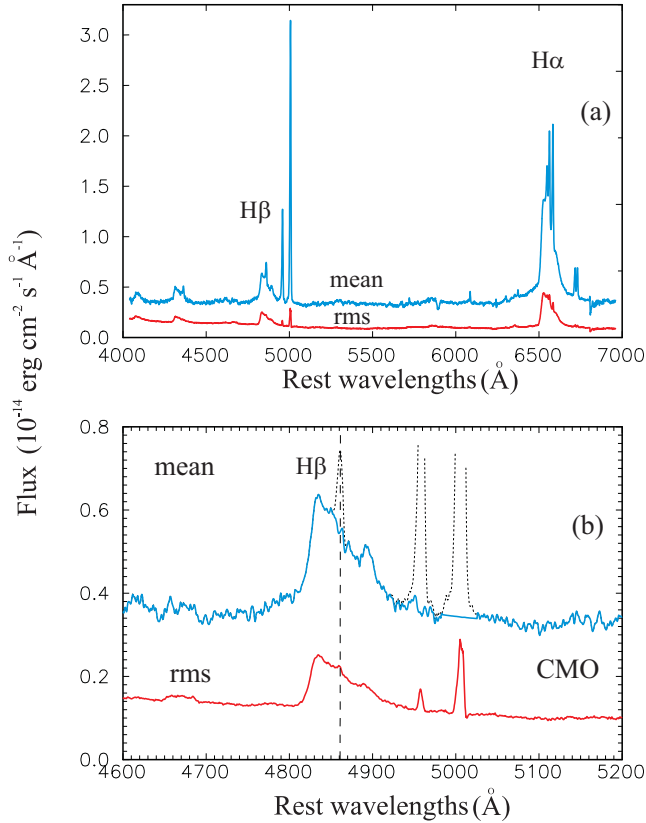


Figure 5. Mean and rms spectra (CMO) in the rest-frame for the full spectral region (a) and just for the H β region (b). In the bottom panel the dotted lines are the narrow H β and [OIII] λ 4959,5007 in the mean spectrum (see more details in the text), while the dashed line indicates 4861 Å in order to illustrate the asymmetric H β profile more clearly.

integration in the same way as it was done with the CMO spectral data.

Fig. 9 shows spectra of the H β region for minimum and maximum fluxes (18 Nov. 2018 and 30 Apr. 2020) for our WIRO observations, as well as the difference spectrum, and the areas of integration for I(H β), I(H β (Blue)) and I(H β (Red)).

The continuum flux in the WIRO data for each spectrum was estimated as the median value in the region 5075 – 5125 Å. We have found a high correlation coefficient between the CMO and the WIRO data ($r > 0.9$) for the H α and H β line variations. Since observations were carried out using instruments of different apertures, the [O III] λ 5007 flux was about two times larger in the WIRO data than in the CMO. Fig. 10 shows combined light curves of the WIRO and CMO data for H α , H β and the continuum reduced to the same system as that of the CMO spectral data and also fluxes based on photometry $I(U)$ (using a linear least squares regression). The WIRO spectral data are presented in Table 4.

3 LIGHT CURVES AND TIME SERIES ANALYSIS

3.1 Light curves

As can be seen from the light curve since 1999 (Fig. 1), NGC 3516 was on average significantly brighter in 1999-2012 than in 2013-2019. After a maximum in 2007 (high state), the brightness of the object decreased to a minimum in 2014 (when the CL event was

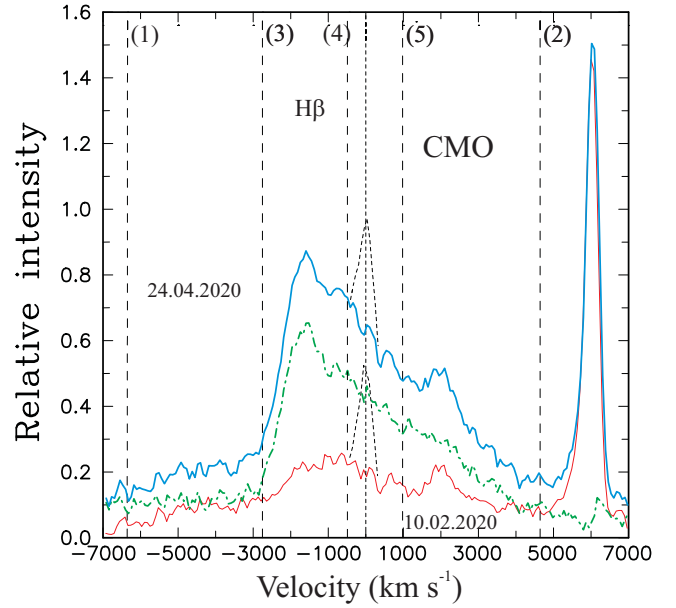


Figure 6. Profiles of broad H β for the maximal (24.04.2020) and minimal (10.02.2020) states (with the narrow components removed) showing intrinsic variations of the line. The difference between the maximal and minimal states is shown by the dash-dotted line. The vertical dashed lines (1-5) mark the regions for integration of I(H β) (1-2), I(H β (Blue)) (3-4) and I(H β (Red)) (5-2). See text for details.

discovered by Shapovalova et al. (2019)). After that, the object was in the low state, but from the end of 2015 to the middle of 2016 some re-brightening was observed. A new CL event corresponding to this high state was observed by Oknyansky et al. (2020a). After this episode, the object was very low again for about 3 years. The relative amplitude of the variability in the optical bands was small, largely due to the relatively large contribution from the host galaxy light within the aperture. The moderate optical variability during this period corresponded to a much more significant variability in the UV, which is explained in part by lower contamination in this wavelength region from the host galaxy.

The optical continuum and Balmer line light curves (see Fig. 10) for 2018-2020 show two epochs of brightening: the first one, at the beginning of 2019, was relatively small, and the second one, which started after a deep minimum at the end of January 2020 and continued till July 2020, was very strong. That strong brightening was accompanied by a significant enhancement of the broad emission lines and variability of their profiles (see Fig. 6,9). During the spring of 2020, several fast flares were observed in all wavelengths (from optical to X-ray) on a timescale of a few weeks. As can be seen from Fig. 2 the variations in B , U , and $UVW2$ in Feb.-Jun. 2020 took place synchronously without any obvious differences. The maxima of these flares were recorded at the all wavelengths from the optical to X-ray. The maxima reached in X-rays (on 2 Mar. and on 1 Apr.2020) were followed by the maxima in UV and optical bands some 1-2 days later. At the maximum (on 1 Apr. 2020) the X-ray flux reached the highest level over the entire history of observations of this object by Swift (nearly 22 times brighter than at the minimal observed level on 27 Jun. 2014). After the maximum, the brightness of the object began to weaken in X-rays but continued to grow in UV/optical bands till the middle

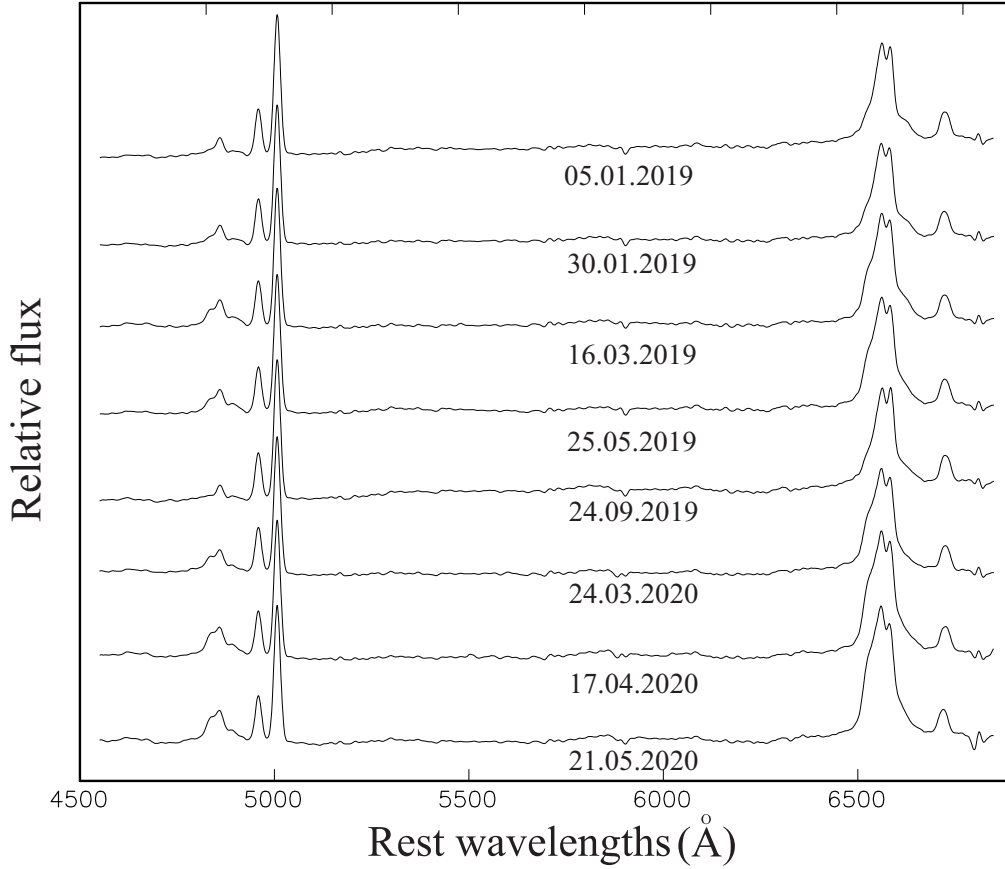


Figure 7. The selected host-galaxy subtracted spectra, obtained in the WIRO for those spectra covering the H α and H β regions. All spectra are normalized to the [O III] λ 5007 intensity and shifted for comparison.

Table 4. Results of optical spectroscopy with the 2.3-m WIRO telescope. (Note: The full version of this table is available in its entirety in machine-readable form.)

J.D.-2450000	H α *	H β *	H β (Blue)*	H β (Red)*	Cont5100 ^a
8438.90	3.42 \pm 0.34	0.76 \pm 0.04	0.20 \pm 0.02	0.27 \pm 0.03	1.62 \pm 0.08
8442.01	3.46 \pm 0.35	0.68 \pm 0.03	0.18 \pm 0.02	0.22 \pm 0.02	1.60 \pm 0.08
8442.94	3.45 \pm 0.35	0.71 \pm 0.04	0.20 \pm 0.02	0.24 \pm 0.02	1.62 \pm 0.08
8443.98	3.04 \pm 0.30	0.68 \pm 0.03	0.19 \pm 0.02	0.22 \pm 0.02	1.56 \pm 0.08
8444.88	3.34 \pm 0.33	0.37 \pm 0.02	0.09 \pm 0.01	0.13 \pm 0.01	1.57 \pm 0.08
...

* Flux value reduced to the CMO system relative to [O III] λ 5007 which mean-weighted flux is 2.2×10^{-13} erg cm $^{-2}$ s $^{-1}$.

^a Flux in continuum at 5100 Å in 10^{-14} erg cm $^{-2}$ s $^{-1}$ Å $^{-1}$ units.

of Apr. 2020. So, we have detected uncorrelated changes in X-rays and the UV/optical continuum in Apr.- Jul. 2020.

The visual analysis of the variations of broad H β during this 7 month period (Dec. 2019–Jul. 2020) shows that the line follows the variations of the continuum but with a delay of about 2-3 weeks (see Fig. 2). Such a strong increase in H β observed on 22 Mar. corresponds to the maximum at the beginning of Mar. 2020. The strong maximum observed in the line at the end of April 2020 corresponds to the maximum in the continuum at the beginning of April. The minimum of the line flux on 10-16 Feb. 2020 corresponds to the minimum of the continuum at the end of Jan. 2020. The local maximum of the line on 17 Jan. 2020 echoes the continuum maximum of 3 Jan. 2020. These visual impressions are confirmed quantita-

tively by our RM results produced by three different methods that are in good agreement (see details below).

3.2 Reverberation mapping methods

To investigate possible lags between variations in the spectral lines and continuum, we used three different RM methods commonly used in the literature: ICCF (traditional interpolation cross-correlation techniques (Gaskell & Sparke 1986; Peterson et al. 1998; Peterson 2004)), MCCF (which is a modification of ICCF (Oknyanskii 1993)), and an alternative method of measuring reverberation time lags - JAVELIN (Bayesian analysis (Zu et al. 2011, 2013)) – formerly known as Stochastic Process Estimation

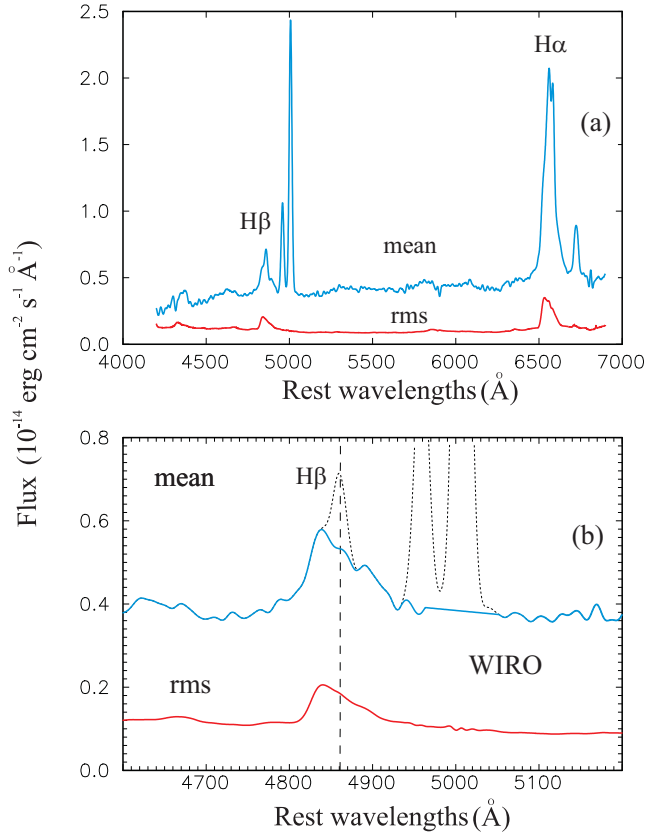


Figure 8. Mean and rms spectra (WIRO) in the rest-frame for the full spectral region (a) and just for the $H\beta$ region (b). In the bottom panel the dotted lines are the narrow $H\beta$ and $[OIII]\lambda 4959,5007$ in the mean spectrum (see more details in the text), while the dashed line indicates 4861 \AA in order to illustrate the asymmetric $H\beta$ profile more clearly.

for AGN Reverberation (SPEAR). All these methods have been used many times (see e.g., Du et al. 2014; Grier et al. 2012; Li et al. 2019; Oknyansky et al. 2017, 2019b). MCCF and ICCF are very similar; MCCF is a modernisation of ICCF to reduce the interpolation errors. In MCCF we used only those interpolated points that were separated in time from the nearest observation points by no more than a limit value $MAX=5$ days. For interpolation we used just one data set that had better accuracy and higher time-cadence. ICCF is more often used in publications and we implemented a publicly available PyCCF code (Sun et al. 2018), adapted from the original ICCF code (Peterson et al. 1998). In both methods, ICCF and MCCF, the errors of time delays were estimated in the same way following Peterson (2004). JAVELIN is also very popular and we used it in the same way as it was discussed in our previous publications (e.g., Oknyansky et al. 2017, 2019b).

Using these techniques, the lag between $X(t)$ and $Y(t)$ can be estimated in at least two ways: from τ_{peak} corresponding to maximum correlation in ICCF and MCCF or equivalently the number N in the histogram (JAVELIN), and from the centroid τ_{cent} (see e.g., Oknyansky et al. 2017). The discussion and references on difference and advantages of ‘peak’ and ‘centroid’ estimations can be also found in Peterson (2004). We prefer to use τ_{peak} when we have principal peaks in the cross-correlation functions well defined and isolated, since it depends on fewer free parameters. The results of our RM (MCCF and JAVELIN) are partially presented in Figs. 11-

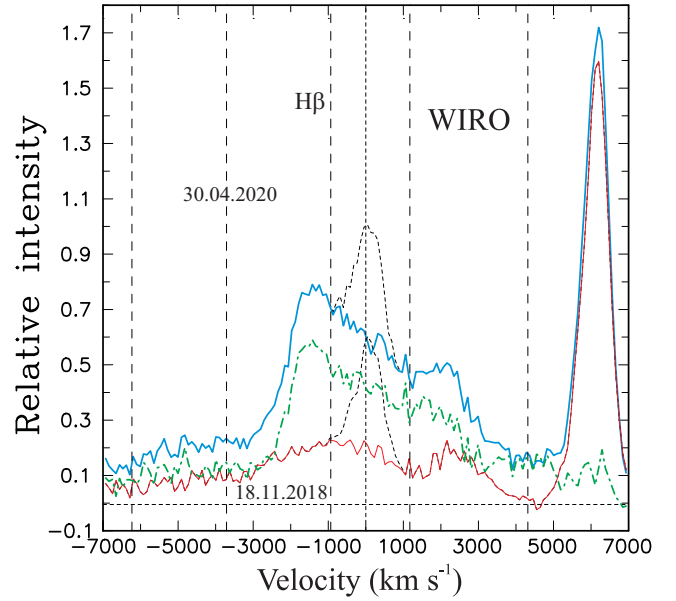


Figure 9. Profiles of broad $H\beta$ for the maximal (30.04.2020) and minimal (18.11.2018) states (with the narrow components removed) showing intrinsic variations of the line. The difference between the maximal and minimal states is shown by the dash-dotted line. The vertical dashed lines (1-5) mark the regions for integration of $I(H\beta)$ (1-2), $I(H\beta(\text{Blue}))$ (3-4) and $I(H\beta(\text{Red}))$ (5-2). See text for details.

14, whereas all the results obtained with three different methods are collected in Table 5.

3.3 Time delay measurements

The emission-line time lags multiplied by the speed of light (c) provide the emissivity-weighted size scales of the regions corresponding to the variable broad lines. In case of time lags associated with the broadband X-ray/UV/optical continuum responses, they may correspond to an effective radius of an accretion disk (although there may be a component of continuum from the broad line region (BLR) as well (see e.g., Korista & Goad 2001).

The RM for continuum flux variations in the optical (U) and $UVW2$ bands confirms the results of visual inspection – these variations show a very high correlation with a maximum of $r \sim 0.97$ near zero lag. However a small possible time shift (~ 0.5 days) between these variations was found by MCCF and JAVELIN (see Table 5), although the confidence of this result is not high due to relatively large gaps in the *Swift* observations. The X-ray flux variations correlate well with the optical ones in the interval 19 Feb.-10 Apr. 2020 ($r \sim 0.87$) with a delay of about 1-2 days, but the correlation drops if all the X-ray data through the end of June 2020 are included. Unfortunately, there are not enough X-ray data to provide a high level of confidence for this result. The variation of the X-ray flux was ahead of the $I(UVW2)$ variations by ~ 1.6 days during 8 Apr. 2012- 10 Apr. 2020. That is in agreement with the result published by Buisson et al. (2017) who used in part the same *Swift* data. That is also in agreement with another published estimate (Noda et al. 2016) of the delay of about 2 days between the optical and X-ray variations.

Our RM analysis was done independently for the CMO and WIRO spectral data with our CMO photometry, as well as for the combined light curves using our three different methods. We inves-

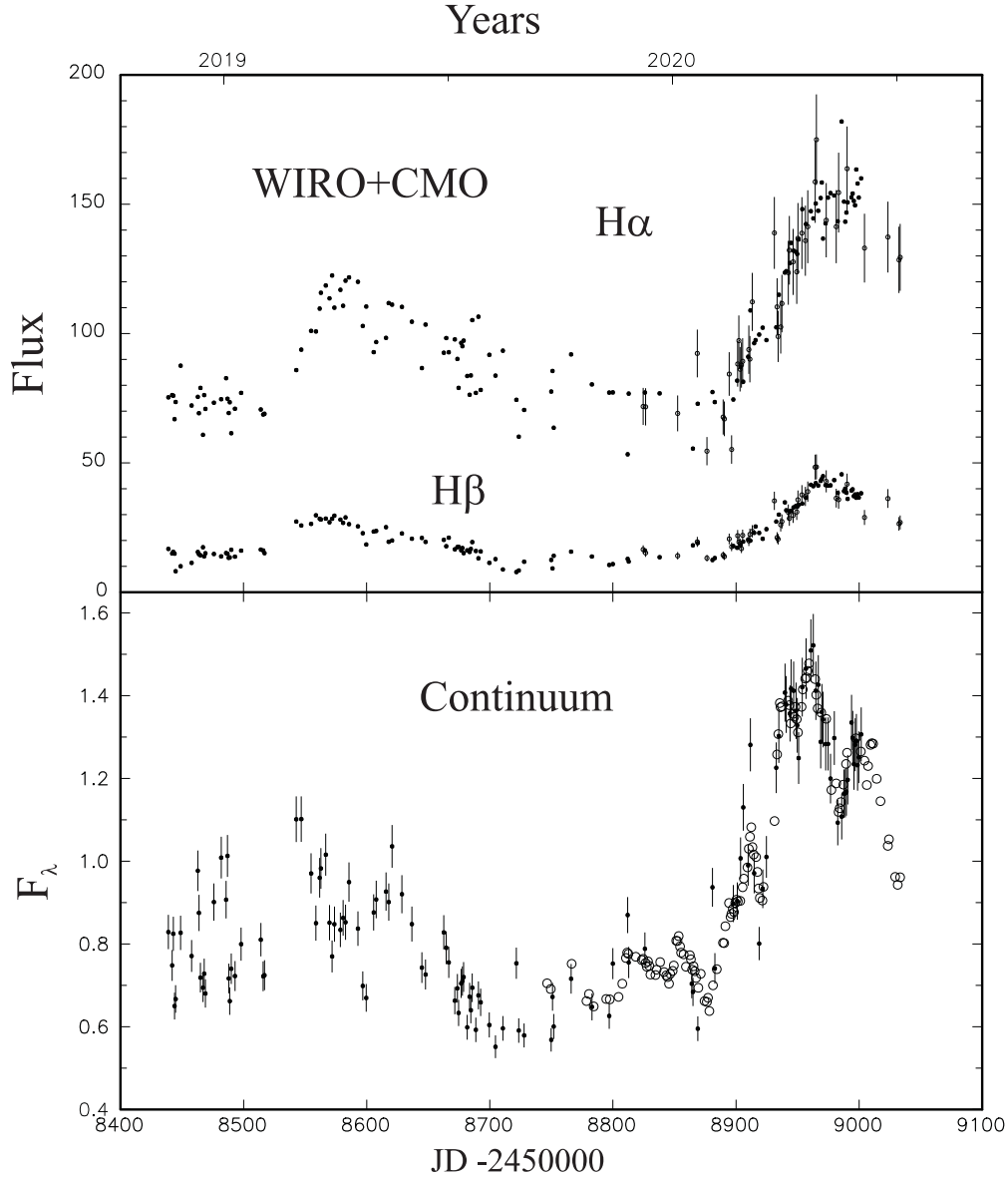


Figure 10. Combined H α , H β and continuum (WIRO and CMO) light curves given in fluxes (in units 10^{-14} erg s $^{-1}$ cm $^{-2}$ for lines and 10^{-14} erg s $^{-1}$ cm $^{-2}$ Å $^{-1}$ for continuum). The CMO data are shown as open circles, the WIRO data as dots. The errors for CMO continuum (from photometry) are not larger than the size of circles. The error bars are shown just for the WIRO continuum values and the CMO H α and H β data. The errors for WIRO spectral data are not shown. See text for details.

tigated time delays relative to the continuum variation not only for different broad emission lines (Balmer lines, He II), but also for the blue and red wings of H β independently.

A quick inspection of Figs. 11–14 and Table 1 confirms that the results obtained with these different methods correspond well with one another. MCCF and ICCF give very similar results for the case when we have well sampled light curves. Some possible differences in the lags obtained with JAVELIN and ICCF have been discussed many times (see e.g., Lira et al. 2015). For the rest of this section, we will refer in the text only to τ_{peak} obtained with the MCCF, but all the results can be found in Table 5.

Fig. 11 demonstrates the MCCF (top panel) and JAVELIN results (bottom panels) for H β , H γ and He II λ 4686 relative to optical continuum I(U) using just the CMO data. The time delays are well defined for these RM results. The H β variations lag by about 17

days (see Table 3 for details and error values). H γ has a smaller delay of about 15 days, although the difference is not very significant. He II has the smallest delay of about 3 days. These relative time delays are seen independently in the MCCF, ICCF and JAVELIN results.

RM for H β (Blue) and H β (Red) relative to optical continuum I(U) is presented in Fig. 12 (just for the CMO data) and Fig. 13 (the WIRO spectral data and the CMO continuum data). Both pictures provide consistent evidence that the blue wing’s delay is about two times longer than that of the red one (about 17 and 9 days, respectively). We note that the CMO photometry started in Sep. 2019, but spectral monitoring began in Dec. 2019. The WIRO monitoring started in Nov. 2018 and finished at the end of May 2020. So, RM for the CMO and WIRO data corresponds for slightly differ-

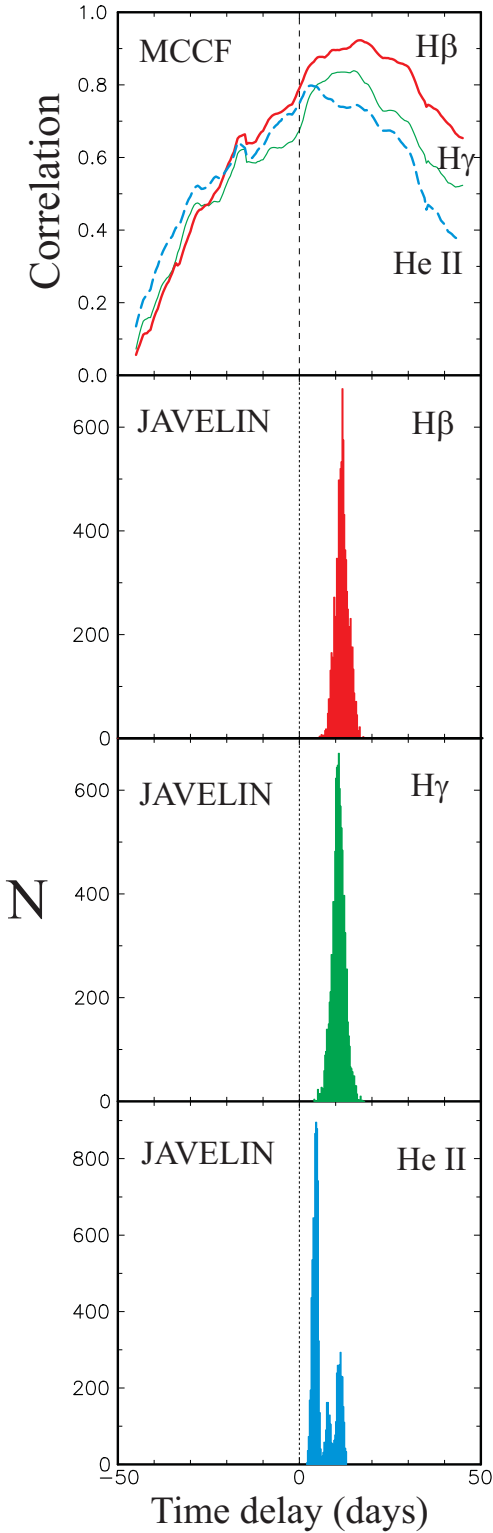


Figure 11. Top panels: RM by the MCCF method (just for the CMO data) for H β (solid line), H γ (thin line) and He II λ 4686 (dashed line) relative to optical continuum $I(U)$. Bottom panels: RM by JAVELIN using the same data. The histograms are shown for each of these lines independently. The vertical dashed lines indicate zero lag.

ent time intervals (Dec. 2019–Jul. 2020 and Sep.2019–May 2020, respectively).

RM for combined H α and H β data relative to combined optical continuum $I(U)$ is presented in Fig. 14. The maximum correlation coefficients are very high. H α probably has a longer delay than H β (about 20 and 17 days, respectively). In Fig. 15 we show the light curve for H β (Blue) and H β (Red)(just the CMO data) shifted by -17 and -9 days and reduced by linear regression to the scale of $I(U)$. The correlation between the continuum and the blue wing of the line with a time delay of about 17 days is clearly seen from the plot.

4 BROAD EMISSION LINE PROFILE VARIATIONS: IMPLICATIONS FOR THE BLR DYNAMICS AND THE BLACK HOLE MASS

A large variation in H β intensity was accompanied by a significant change in the line profile. The examples of H β profiles for the maximum and minimum states are presented in Fig. 6 (CMO) and Fig. 8 (WIRO). The profiles of H β in the high state are asymmetric and double-peaked with the blue peak dominating. The asymmetry was stronger in the maximum state during April–May 2020. This fact is clearly seen in Fig. 16 where the light curves of H β (Blue) and H β (Red) are shown shifted by -17 and -9 days, respectively. There are also present the variations of the ratio of H β (Red) / H β (Blue) to show variability of the line asymmetry.

We have found not only considerable variations in the H β , H α , H γ , He II λ 4686 lines, but the appearance of strong Balmer continuum in the high state, too (see Fig. 3), which is a typical feature for the CL AGN (see e.g., Shappee et al. 2014; Oknyansky et al. 2020b). We have also detected prominent coronal lines and possible variations of these lines that is also indicative of a CL event. The details on the variability of the coronal lines will be given in our future publication. In this work, we report on a strong outburst in NGC 3516 and on the recovering of the object back to the high state, which is similar to the previous CL event in 2016 (Oknyansky et al. 2020b).

The time delay of about $\tau \sim 19$ days (taking into account the 2 days delay for the optical from X-ray variations) found for H β ($R_{BLR} = c\tau$ is the emissivity-weighted radius of the BLR) and the full-width-half-maximum (FWHM) of the line rms-profile of about 4700 km s^{-1} can be used to estimate the virial black hole (BH) mass:

$$M_{BH} = f \frac{R_{BLR} \Delta V^2}{G}, \quad (1)$$

where G is the gravitational constant and f is the virial factor determined by the geometry and kinematics of the BLR (e.g., Peterson 2004). Adopting the recent value for the f factor from Woo et al. (2015) who obtained $\log f = 0.05 \pm 0.12$ for the FWHM-based M_{BH} estimates, we obtain a mass of $\sim 5 \times 10^7 M_{\odot}$ for the central BH. This value is generally consistent with similar virial H β -based RM estimates published by Peterson (2004) based on data from Wanders et al. (1993) of $4.27 \pm 1.46 \times 10^7 M_{\odot}$; Denney et al. (2010) of $3.17^{+0.28}_{-0.42} \times 10^7 M_{\odot}$; De Rosa et al. (2018) of $4.27^{+1.48}_{-1.11} \times 10^7 M_{\odot}$; Shapovalova et al. (2019) of $4.73 \pm 1.40 \times 10^7 M_{\odot}$; Feng et al. (2021b) of $2.4^{+0.7}_{-0.3} \times 10^7 M_{\odot}$; and with the mass of $(1 - 5) \times 10^7 M_{\odot}$ obtained using the variability of the Fe K α X-ray line reported by Iwasawa et al. (2004). The high precision of the above values reflects measurement errors, while systematic errors due to issues of choice of measurement algorithm, calibration of

Table 5. Results from the RM analysis. Lags for X data sets are measured with respect to the Y data and are expressed in days. A positive lag means the Y set leads the X variability. For MCCF the correlation values in the peak R_{max} are given. For interpolated MCCF and ICCF 1σ confidence limits and centroids for interpolated cross-correlations are presented. For JAVELIN confidence limits are measured at a 95% confidence level. Our preferred τ_{peak} values obtained by MCCF are given in bold. All delays are reduced to the rest system.

X	Y	J.D.-2450000	Date	MCCF			ICCF		JAVELIN
				R_{max}	τ_{peak}	τ_{cent}	τ_{peak}	τ_{cent}	τ_{peak}
I(U) (CMO)	I(B) (CMO)	8746–9033	Sep.2019–Jul.2020	0.998	0.4^{+0.2}_{-0.1}	0.4 ^{+0.3} _{-0.3}	0.4 ^{+0.2} _{-0.1}	0.2 ^{+0.5} _{-0.6}	0.2 ^{+0.2} _{-0.1}
I(U) (CMO)	I(UVW2)	8899–9024	Feb.2020–Jun.2020	0.967	0.4^{+0.3}_{-0.1}	0.4 ^{+0.3} _{-0.3}	0.4 ^{+0.1} _{-0.4}	0.0 ^{+0.1} _{-0.4}	0.65 ^{+0.25} _{-0.25}
I(UVW2)	I(X-ray)	6026–8943	Apr.2012–Apr.2020	0.939	1.6^{+0.8}_{-0.6}	1.4 ^{+0.9} _{-0.7}	1.3 ^{+1.6} _{-1.5}	1.5 ^{+1.7} _{-1.8}	1.35 ^{+0.25} _{-0.25}
H α (CMO)	I(U) (CMO)	8824–9033	Dec.2019–Jul.2020	0.919	16.9^{+0.6}_{-0.5}	16.6 ^{+0.7} _{-0.5}	18.4 ^{+4.5} _{-3.8}	18.6 ^{+3.9} _{-3.6}	17.1 ^{+1.1} _{-1.1}
H α (WIRO)	I(U) (CMO)	8749–9001	Sep.2019–May 2020	0.920	20.9^{+6.0}_{-7.0}	18.8 ^{+6.4} _{-6.0}	18.9 ^{+6.6} _{-6.2}	19.7 ^{+4.1} _{-4.0}	19.1 ^{+2.8} _{-2.8}
H β (CMO)	I(U) (CMO)	8824–9033	Dec.2019–Jul.2020	0.958	16.7^{+3.5}_{-4.0}	15.9 ^{+3.4} _{+4.4}	14.9 ^{+1.9} _{+4.6}	15.0 ^{+4.1} _{+4.2}	11.8 ^{+3.1} _{-3.1}
H β (WIRO)	I(U) (CMO)	8749–9001	Sep.2019–May 2020	0.953	15.3^{+2.2}_{-2.0}	14.0 ^{+2.4} _{-3.4}	18.2 ^{+1.8} _{-6.2}	15.9 ^{+2.2} _{-2.7}	14.9 ^{+1.1} _{-1.1}
H γ (CMO)	I(U) (CMO)	8824–9033	Dec.2019–Jul.2020	0.839	14.9^{+2.0}_{-5.0}	12.2 ^{+2.4} _{+5.4}	12.5 ^{+5.8} _{-1.3}	14.2 ^{+8.5} _{-4.6}	11.2 ^{+3.0} _{-3.0}
He II (CMO)	I(U) (CMO)	8824–9033	Dec.2019–Jul.2020	0.798	3.2^{+2.5}_{-2.5}	0.36 ^{+4.0} _{+5.0}	3.7 ^{+6.8} ₋₁₀	5.7 ^{+7.0} _{-9.7}	4.5 ^{+1.0} _{-2.0}
H β (Blue) (CMO)	I(U) (CMO)	8824–9033	Dec.2019–Jul.2020	0.956	16.9^{+2.0}_{-1.5}	15.8 ^{+2.4} _{-2.0}	16.8 ^{+4.0} _{-0.8}	19.3 ^{+5.3} _{-4.1}	15.7 ^{+2.1} _{-2.0}
H β (Blue) (WIRO)	I(U) (CMO)	8749–9001	Sep.2019–May 2020	0.965	21.4^{+2.0}_{-2.4}	19.1 ^{+2.4} _{-2.4}	21.9 ^{+2.1} _{-2.1}	20.9 ^{+3.4} _{-2.1}	16.0 ^{+2.1} _{-2.1}
H β (Red) (CMO)	I(U) (CMO)	8824–9033	Dec.2019–Jul.2020	0.902	8.9^{+2.0}_{-5.0}	7.9 ^{+3.0} _{-4.0}	8.6 ^{+5.4} _{-2.7}	10.6 ^{+3.8} _{-4.0}	7.7 ^{+1.0} _{-3.0}
H β (Red) (WIRO)	I(U) (CMO)	8749–9001	Sep.2019–May 2020	0.918	6.1^{+1.6}_{-2.2}	5.7 ^{+2.4} _{-2.4}	5.1 ^{+6.3} _{-2.4}	9.4 ^{+1.6} _{-0.6}	6.7 ^{+1.0} _{-1.2}
H α (CMO+WIRO)	I(U) (CMO+WIRO)	8438–9033	Nov.2018–Jul.2020	0.895	21.2^{+2.8}_{-1.8}	18.0 ^{+3.4} _{-1.4}	20.0 ^{+2.5} _{-3.9}	20.8 ^{+3.0} _{-2.7}	19.7 ^{+2.8} _{-0.7}
H β (CMO+WIRO)	I(U) (CMO+WIRO)	8438–9033	Nov.2018–Jul.2020	0.931	17.5^{+1.9}_{-1.7}	15.9 ^{+2.0} _{-1.4}	17.3 ^{+2.2} _{-2.3}	15.5 ^{+4.0} _{-2.1}	16.6 ^{+0.5} _{-0.2}

the f factor and its deviation from the average (e.g., Pancoast et al. 2014), as well as the choice of method for measuring the velocity ΔV (e.g., Dalla Bontà et al. 2020), make the masses much more uncertain.

We want to point out that the very recent results of Feng et al. (2021b) were based on a six-month campaign from November 2018 to May 2019 that covered the epoch of the first and fainter of the two brightenings we also observed. They found time lags generally smaller than ours (~ 7.5 days in the case of H β), which is not unexpected given the lower average luminosity; different RM campaigns listed above have found H β time lags of ~ 1 -3 weeks. Our time lags are dominated by the much larger variation in the second, larger brightening and are closer to the longer delays reported. Both our measurements and those of Feng et al. (2021b) find the same dynamics, with similarly longer time delays for the blue side of the H β profile, but the difference is that during the second brightening the blue side strengthened much more than the red side (Fig. 16). The blueshifted emission region on the far side of the BLR would then perhaps be more clearly seen than red-shifted gas on the closer side of the BLR, due to opacity and asymmetric emission preferentially back toward the continuum source.

These considerations suggest radial infall rather than orbital motion. Orbital motion of gas in a flattened disk has often been preferred in other objects with double-peaked profiles that show symmetric velocity-resolved time lags. The profile asymmetries and much longer time lags on the blueside suggest an alternative to a flattened disk with orbiting clouds. Let us consider a simple model with two-sided symmetrical radial inflows with effective luminosity-weighted centres located at the distance R_{in} from the central BH in the direction that forms an angle δ to the line of sight. In this case, the time delay (luminosity-weighted) for the emission region responsible for the blue peak will be $\tau_{bl}c = R_{in}(1 + \cos \delta)$ and for the red, $\tau_{red}c = R_{in}(1 - \cos \delta)$. The measured values of $\tau_{bl}=17$ days and $\tau_{red}=9$ days must be increased by 2 days corresponding to

the optical from X-ray delay. Then we can estimate δ as $\sim 75^\circ$ and $R \sim 15$ l.d. The velocity in the maximum in the blue peak of H β is ~ 1700 km s $^{-1}$ corresponding to the radial inflow velocity $V_r \sim 6400$ km s $^{-1}$.

If we assume that this velocity relates to free fall in the gravitation field of the central BH, then by analogy from Equation 1 we get

$$M_{BH} = \frac{R_{in} V_r^2}{2G}. \quad (2)$$

According to Equation 2, the BH has a mass of $\sim 5 \times 10^7 M_\odot$, that agrees well with the estimates above. This is promising in that perhaps the virial equation, commonly adopted for mass estimation when only single-epoch spectra are available, does not provide wildly inconsistent values compared with a likely radial flow producing an extremely asymmetric profile.

5 EVOLUTION OF THE X-RAY SPECTRUM

To trace the evolution of the X-ray spectrum of NGC 3516 as a function of luminosity, we performed analysis of three *Swift*/XRT spectra with large enough exposure (to have about similar signal/noise ratio in each spectrum) obtained in very different states. Particularly, the source was observed in the low state with a flux of $F_{0.5-10\text{keV}} = 7.3 \times 10^{-12}$ erg s $^{-1}$ cm $^{-2}$ on July 11, 2014 (ObsID 00080749004), whereas the maximal flux $F_{0.5-10\text{keV}} = 9.8 \times 10^{-11}$ erg s $^{-1}$ cm $^{-2}$ was observed around April 1, 2020 (ObsID 00035462024).

For comparison we also analysed one set of observational data obtained one month after the maximum when the source was in an intermediate flux state with $F_{0.5-10\text{keV}} = 4.7 \times 10^{-11}$ erg s $^{-1}$ cm $^{-2}$ on May 2, 2020 (ObsID 00035462032). Spectral analysis has been done using xSPEC package (Arnaud 1996) and applying W-statistics

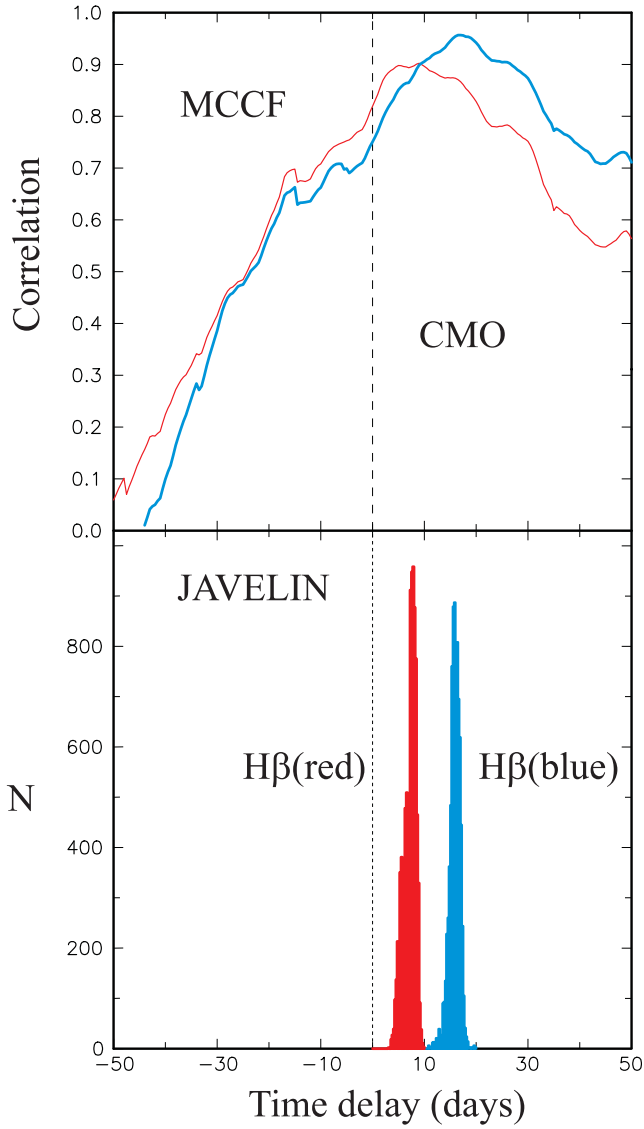


Figure 12. Top panels: RM by the MCCF method (just for CMO data) for H β (blue) (solid line), H β (red) (thin line) relative to optical continuum I(U). Bottom panel: the RM histogram by the JAVELIN using the same data. The vertical dashed lines indicate zero lag.

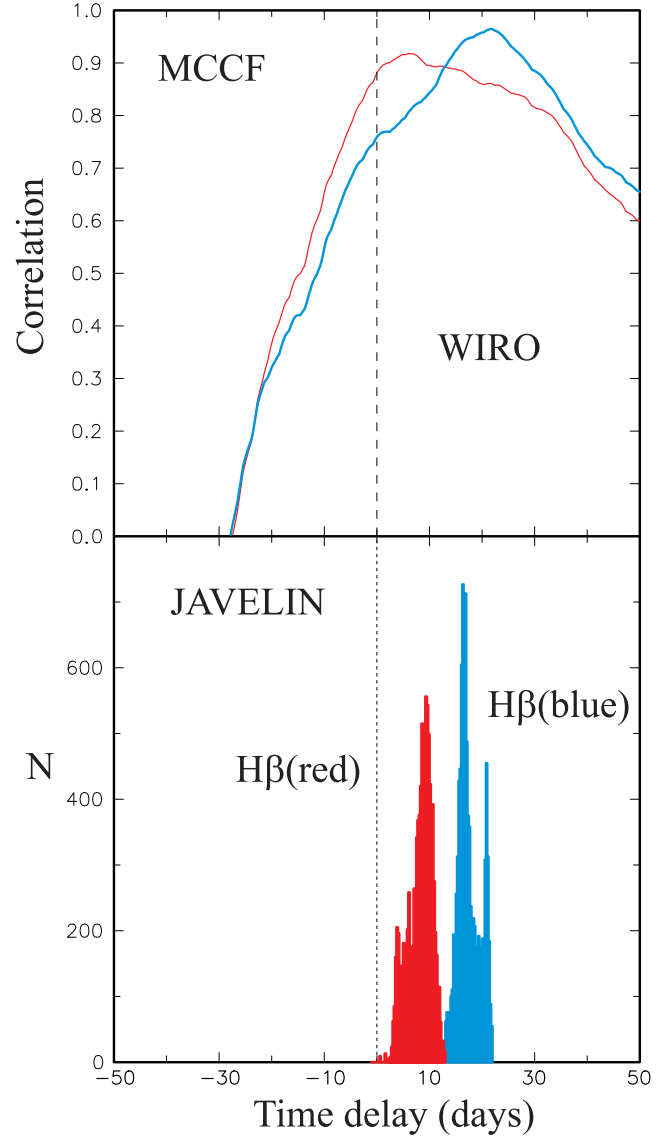


Figure 13. Top panels: RM by the MCCF method (just for the WIRO spectral data) for H β (blue) (solid line), H β (red) (thin line) relative to optical continuum I(U) from the CMO photometry. Bottom panel: the RM histogram by JAVELIN using the same data. The vertical dashed lines indicate zero lag.

(Wachter et al. 1979) after the spectra were binned to have at least one count in each energy channel.

We started our spectral analysis with the simplest model consisting of a power law modified by photoelectric absorption (PHABS×PO models in xSPEC). The residuals for this model shown in Fig. 17b clearly demonstrate an unacceptable fit. Particularly, either a broad absorption between 0.6 and 1.1 keV, or additional soft emission component below 1 keV, is required. Applying this simplified model to all available spectra we derived the equivalent hydrogen column density consistent with zero and photon index ranging from 0.6 to 1.6 for the lowest and highest states, respectively.

As the next step we modified our initial model adding a soft black body component. To take into account the Galactic photoelectric absorption we introduced the second PHABS component and fixed its value at $0.03 \times 10^{22} \text{ cm}^{-2}$ (HI4PI Collaboration et al. 2016). Therefore, the final best-fit model for all the three *Swift*/XRT spec-

tra is PHABS×(BB+PHABS×PO). The second PHABS component represents intrinsic absorption and was left free to vary. The resulting spectra and corresponding spectral parameters are shown in Fig. 17 and Table 6, respectively.

As it is seen from Fig. 17 the change between high and post-maximum intermediate states is about the same for all the energy regions. Such type of variability can be due to either intrinsic continuum variations or ‘colorless’ variability originating from the passage of Compton-thick blobs of gas across the line-of-sight. Taking into account the dropout of the X-ray and UV correlation for the same dates makes the second explanation more plausible.

A significant change of about 2 orders of magnitude of the soft X-ray from the minimal state to the high and intermediate ones rejects the possibility to explain this soft component as thermal radiation from the host galaxy and so the preference should be given

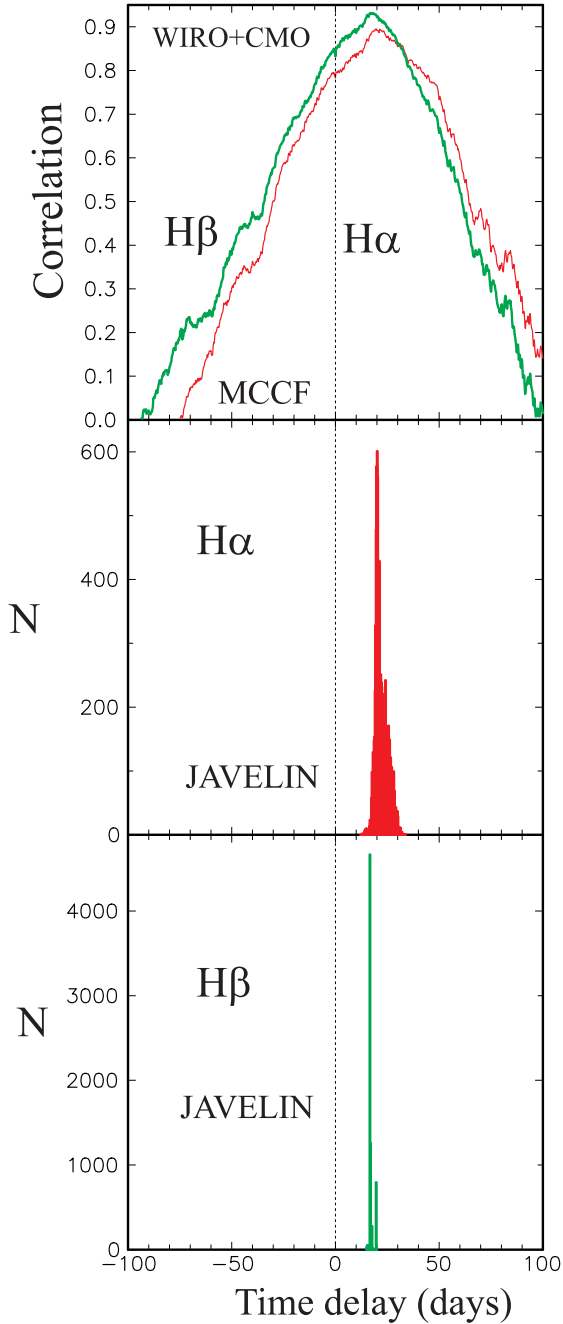


Figure 14. Top panels: RM by the MCF method (for the combined CMO and WIRO data) for $H\beta$ (solid line), $H\alpha$ (thin line) relative to optical continuum (see text). The RM histograms by JAVELIN (using the same data) are shown for $H\alpha$ at the middle panel and for $H\beta$ at the bottom panel. The vertical dashed lines indicate zero lag.

to the models which predict strong variability of the soft excess (e.g., Gardner & Done 2017).

In addition to detailed fits of these three epochs, we measured the photon index power law Γ more generally for the entire Swift XRT data set for NGC 3516 for the simple absorbed power law model. Fig. 18 shows generally small values of Γ when the X-ray flux is low, but there is a significant increase during the 2020 brightening, although falling off at the end. This is consistent with an intrinsic version of the correlation between Γ and Eddington ratio previously reported (e.g., Risaliti et al. 2009). These relatively

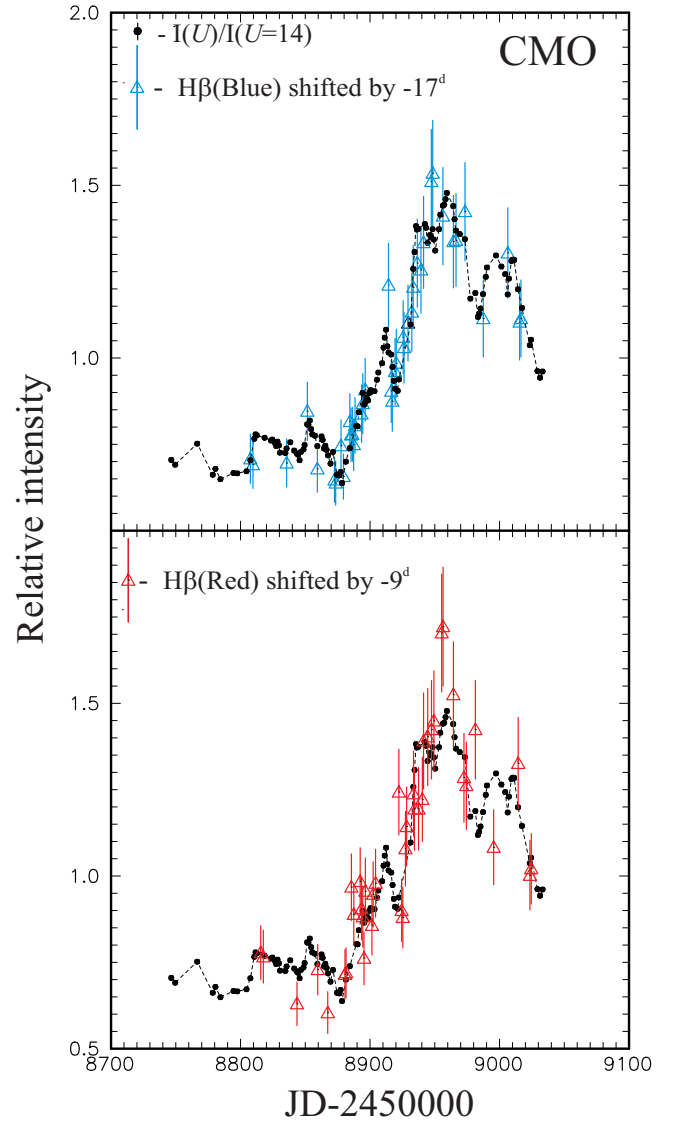


Figure 15. Top panel: Light curves for relative intensity $I(U)$ (Intensity for $U=14$ mag corresponds to 1) and $I(H\beta(\text{Blue}))$ reduced to the $I(U)$ scale by the linear regression and shifted by -17 days. Bottom pane: The same as at the top panel light curves $I(U)$ and $I(H\beta(\text{Red}))$ reduced to the $I(U)$ scale by the linear regression and shifted by -9 days.

small values of Γ are suggestive of low Eddington fractions associated with the transition between different Seyfert classes as seen in NGC 3516.

6 DISCUSSION AND CONCLUSIONS

NGC 3516 is one of the typical examples of an AGN for which spectra range from type Sy1.2 to type Sy1.9 and back for the same object over long time scales (years) or sometimes shorter time scales (months). Using our spectroscopy and multi-wavelength photometry, we have shown that NGC 3516, after several years being in a low state, is recently again in a high state with strong broad emission lines and the highest flux level of its continuum. These dramatic changes can be identified as a new CL event for the object.

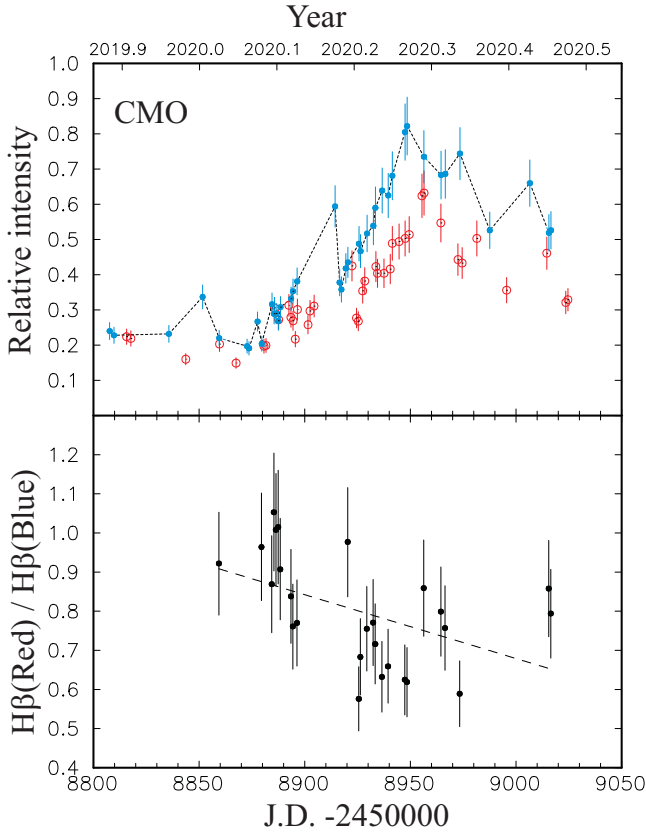


Figure 16. Top panel: Light curves for relative intensity $I(H\beta(\text{Blue}))$ (dots) and $I(H\beta(\text{Red}))$ (open circles) shifted by -17 and -9 days, respectively (The scale was not reduced as at the Fig. 15 and values are the same as in Table 3). Bottom panel: variations of the $I(H\beta(\text{Red})) / I(H\beta(\text{Blue}))$ ratio for the values shifted as it is shown on the top panel. We use just those interpolated values of $I(H\beta(\text{Red}))$ which are farther not more than 2 days from the nearest observation.

We have found delays between continuum variations at different wavelengths (X-ray, UV, optical), as well as delays between continuum and broad emission lines variability using 3 different statistical methods. The wavelength-dependent time-delays between the continuum at different wavelengths are predicted in the most common standard model with the thermal reprocessing hypothesis in AGN, where extreme ultraviolet/X-ray photons are reprocessed by the accretion disc (AD) into optical/UV photons (Cackett et al. 2007, see e.g.,). In this model it is assumed that the X-ray emitter is located on the rotating axis of the supermassive black hole (SMBH) like a “lampost” and its height H_x from the SMBH is much smaller than R – distance to the location where the UV/optical radiation arises in AD. Our inference that the UV variations lag behind the X-ray ones by ~ 1.6 days (which is in agreement with previously published results Buisson et al. (2017); Noda et al. (2016)) is in contradiction with the lampost-type X-ray reprocessing model, that is a common problem for other typical Seyfert galaxies (which are mostly also known as CL AGNs) including NGC 4151, NGC 5548, NGC 4051, NGC 2617, NGC 1566, and Mrk 335 (see e.g., Cackett et al. 2007; Buisson et al. 2017; Edelson et al. 2017; McHardy et al. 2014; Shappee et al. 2014; Oknyansky et al. 2017, 2020b). For some gravitationally lensed quasars the sizes of ADs measured from the microlensing data are also significantly larger than those predicted by the

Table 6. Best-fit parameters for a $\text{PHABS}\times(\text{BB}+\text{PHABS}\times\text{PO})$ model obtained for three *Swift*/XRT observations. All errors are reported at 1σ confidence level.

Parameter	Units	Value
High state (ObsID 00035462024)		
$N_{\text{H}1}$	10^{22} cm^{-2}	0.03^a
kT^b	keV	0.11 ± 0.02
Norm _{bb}	$L_{39}/D_{10\text{kpc}}^2$	$(4.6 \pm 0.8) \times 10^{-4}$
$N_{\text{H}2}$	10^{22} cm^{-2}	0.3 ± 0.2
Power-law ph. index		1.8 ± 0.3
Power-law norm.		$(1.9 \pm 0.8) \times 10^{-2}$
Flux ^c	$10^{-11} \text{ erg s}^{-1} \text{ cm}^{-2}$	9.8 ± 0.2
Intermediate state (ObsID 00035462032)		
$N_{\text{H}1}$	10^{22} cm^{-2}	0.03^a
kT^b	keV	0.10 ± 0.01
Norm _{bb}	$L_{39}/D_{10\text{kpc}}^2$	$(1.8 \pm 0.3) \times 10^{-4}$
$N_{\text{H}2}$	10^{22} cm^{-2}	0.32 ± 0.15
Power-law ph. index		1.8 ± 0.2
Power-law norm.		$(1.0 \pm 0.2) \times 10^{-2}$
Flux ^c	$10^{-11} \text{ erg s}^{-1} \text{ cm}^{-2}$	4.7 ± 0.2
Low state (ObsID 00080749004)		
$N_{\text{H}1}$	10^{22} cm^{-2}	0.03^a
kT^b	keV	0.18 ± 0.03
Norm _{bb}	$L_{39}/D_{10\text{kpc}}^2$	$(6.4 \pm 0.8) \times 10^{-6}$
$N_{\text{H}2}$	10^{22} cm^{-2}	1.3 ± 0.5
Power-law ph. index		1.2 ± 0.3
Power-law norm.		$(8.5 \pm 3.0) \times 10^{-4}$
Flux ^c	$10^{-12} \text{ erg s}^{-1} \text{ cm}^{-2}$	7.3 ± 0.3

^a Fixed.

^b Black body temperature.

^c Observed flux in the 0.5–10 keV energy band.

most commonly adopted X-ray reprocessing model (e.g., Morgan et al. 2010). First of all, the observed luminosity (estimated Eddington ratios) has to be much higher for the size of the accretion disk determined by the observed time lag and microlensing estimations (Cackett et al. 2007). If to take $H_x \sim R$ which is required to explain the observed delays, then the necessity to explain sufficient primary X-ray radiation from such an X-ray corona makes this possibility highly unrealistic (Noda et al. 2016). Two possible alternative models were discussed by Noda et al. (2016) (see details therein) to explain such big lags in UV/optical variation: truncated AD in analogy with black-hole binaries (e.g., Done et al. (2007)) and the model with a soft excess region at the inner edge of an accretion disk which completely hides the hard X-ray corona (Gardner & Done 2017). The second model was also used to explain the time delays in NGC 4151 (Edelson et al. 2017). However, Noda et al. (2016) prefer the truncated AD model for NGC 3516 on the grounds that soft X-ray variations are not detected. Our results indicate strong variability of the soft component, which can not be associated with the host galactic thermal emission. So, our results do not reject the second model. The big values for UV/optical delay can also be explained assuming that some part of the flux arises not from the AD but relates to the diffuse continuum radiated by the same gas that emits the broad emission lines. (see e.g., Goad et al. 2019). For example, a delay in U of about 0.4 days relative to B found by us can be explained by the Balmer continuum input to the band, which is clearly seen in our spectra (see Fig. 3).

We have found a delay of about 17 days for the variation in

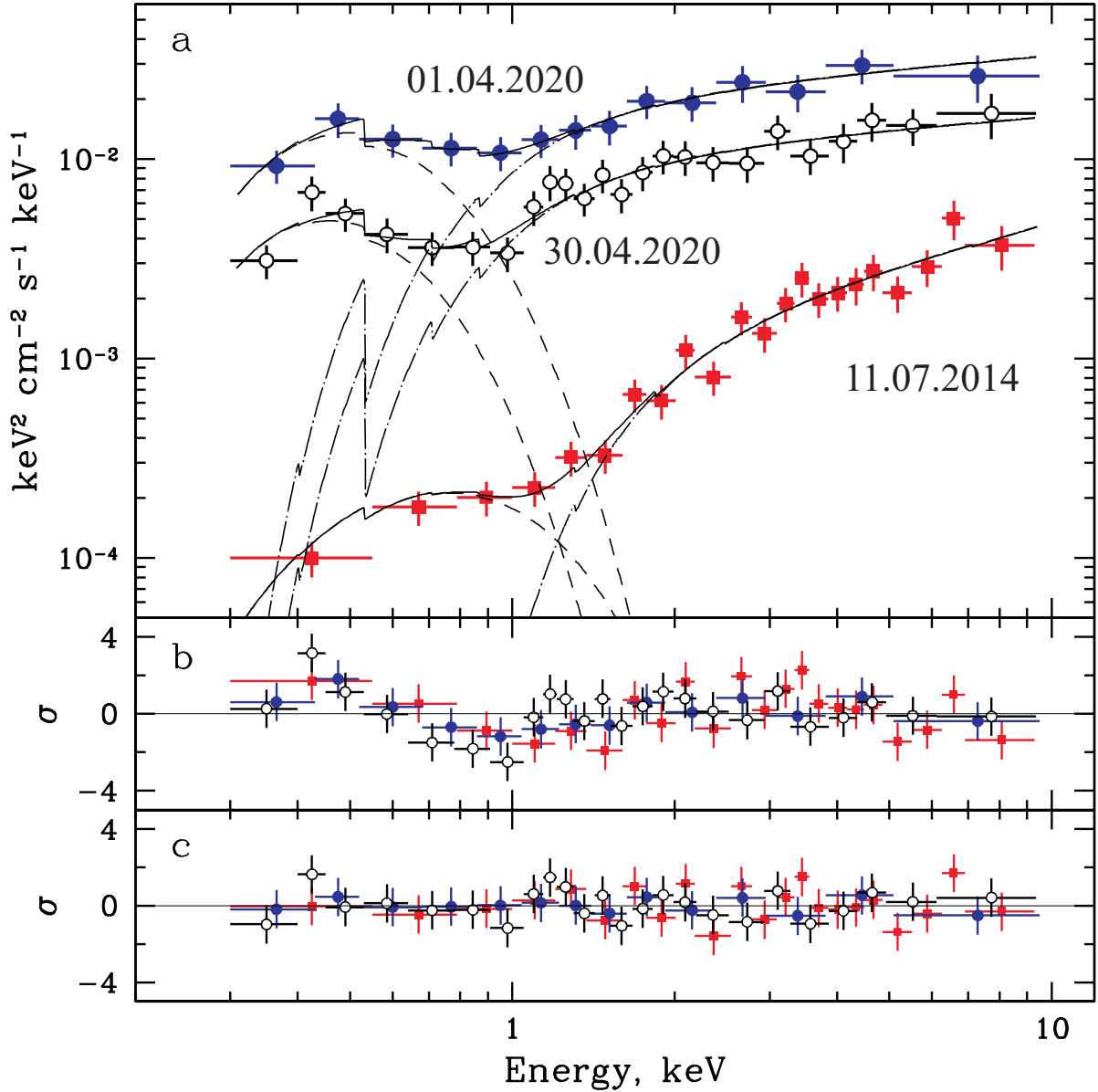


Figure 17. (a) Unfolded X-ray spectra of NGC 3516 obtained with *Swift*/XRT in different states. Spectra in high (ObsID 0003546204), intermediate (ObsID 00035462032) and low (ObsID 00080749004) flux states are shown with solid circles, open circles and solid squares, respectively. Solid line represent the best-fitting model consisting of the absorbed power-law and black body (also shown with dash-dotted and dashed lines, respectively).

$H\beta$ and predicted the variations of the line on the base of optical photometry. We have found the time delays slightly decreased for the Balmer lines from maximal for $H\alpha$ to minimal for $H\gamma$. The same result was found for some other AGNs (e.g., Feng et al. 2021a) and can be due to the decrease of the optical depth along the $H\alpha$, $H\beta$ and $H\gamma$ lines. The time delay for He II was found to be smaller than for all the Balmer lines, as is the case in many other AGNs (e.g., Grier et al. 2013; Peterson et al. 2014) which can be due to the fact that the emission region of higher ionisation is located closer to the central source of the UV ionisation flux. These time delays allow us to estimate the spatial scales corresponding to the emission regions in the BLR.

Double-peaked broad emission line profiles are seen in many AGNs and were intensively investigated both in observational and theoretical ways (see e.g., Strateva et al. 2003; Du et al. 2018). In NGC 3516 the double emission line profile was seen in previous

spectra (Shapovalova et al. 2019) but in our spectra taken in 2019–2020 the emission peaks in the blue and red wings of $H\beta$ are more prominent and the blue one is stronger than the red. Strateva et al. (2003) argued that the situation when the blue peak is stronger than the red could be explained by a circular disc emission model. At the same time, the largest delay for the negative velocities in the $H\beta$ emission may indicate inflowing kinematics of the gas clouds, inconsistent with disc orbital motions. The observed characteristics are about the same as were found in 2007 (Denney et al. 2009), when the object was in the high state and probably are different from those in 2012 (De Rosa et al. 2018) when the object was in the low state. This does not necessarily mean that the kinematics of the clouds have changed in such a short time. This may be due to the fact that when the luminosity of the object changes, the size of the region which effectively radiates in broad emission lines varies, too, and the kinematics of the clouds can depend on the distance

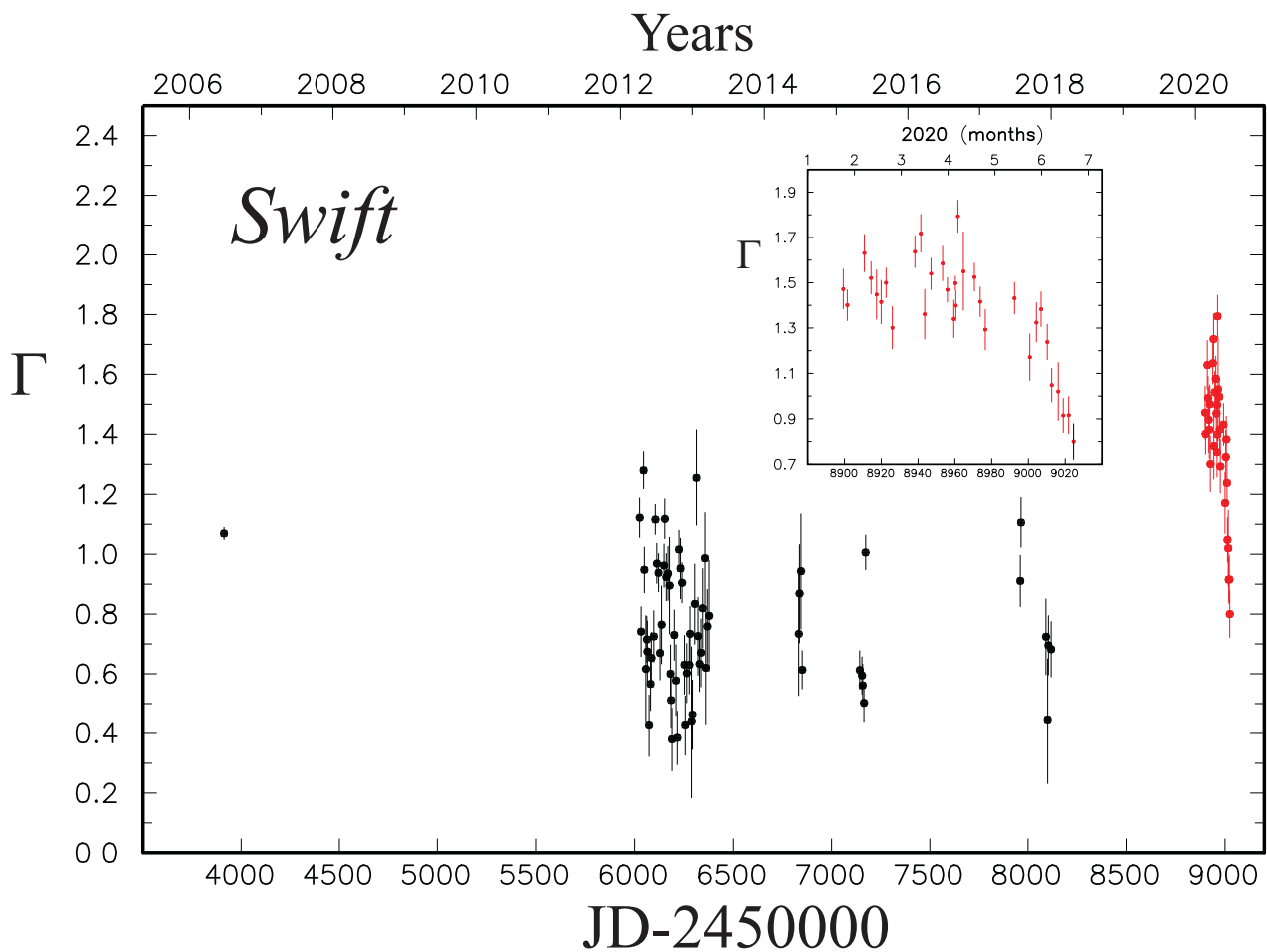


Figure 18. Evolution of the photon index value, calculated by assuming a simple absorbed power-law model, based on the *Swift*/XRT data. The inset shows results obtained during first half of 2020. (See details in the text).

to the central source. The profile of $H\beta$ in Mar.-Jul. 2020 is similar to that observed in 2007. That is in agreement with our conclusion that the object has changed its type back to Sy1.5 again. The CL event observed in 2020 is similar to a previous one that occurred about 4.5 years before (Oknyansky et al. 2019b). This time interval is in agreement with regularity in optical variations of the object found by Kovačević et al. (2020).

Dramatic changes of the optical emission lines followed a strong outburst in the X-rays and UV. On 1 Apr. 2020 the X-ray flux reached a maximal level (since *Swift* observations began in 2006) of about 9.8×10^{-11} ergs $\text{cm}^{-2} \text{s}^{-1}$ that is about 22 times bigger than in the observed minimum on 27 Jun. 2014. This amplitude is compatible with what is seen (20–50 times) in other highly variable CL AGNs (see e.g., Oknyansky et al. 2019a; Zetzl et al. 2018). The amplitude of the UV outburst was about 3 magnitudes, but the maximum was about 3 weeks later than in the X-ray. Variations of X-ray and UV/optical radiation were different during the second half of April – June 2020. At the first date of *Swift* observations in 2006 (see Fig. 1) a high level of UV brightness was observed, but rather intermediate one of X-ray flux, though they were mostly well correlated during 2012–2020. These events of colorless variations of X-ray flux which are not correlated with UV/optical variability might be suggested to be a consequence of Compton-thick clumps of gas crossing the line-of-sight and temporarily obscuring the X-ray source which is significantly smaller than the UV/optical one

(see e.g., for NGC 2617 Oknyansky et al. 2017). A similar event was observed during the previous high state of NGC 3516 in 2009 and the same explanation was invoked by Turner et al. (2011).

The observed change in asymmetry of $H\beta$ in April - May 2020 can also be associated with some absorption (coinciding in time with the proposed absorption in X-ray), which weakened ionizing radiation in the direction of the emission region of the red peak in the line. The presence of absorption predominantly on one side of the AD indicates a certain asymmetry in the distribution of absorbing dense clouds, which can be used for selecting a possible model for CL events.

We offer as an alternative a straightforward explanation of the changes in $H\beta$ profile asymmetries and velocity-resolved time lags observing in NGC 3516. A BLR with a flattened geometry seen more edge-on than face-on will have the near-side respond with shorter time lags than the far side. Moreover, we may expect the side of the line-emitting gas facing the continuum source to emit more strongly and preferentially back in the direction of the continuum, and thus be seen more strongly from our perspective (Pan-coast et al. 2014). If we consider the NGC 3516 BLR to be dominated by radial motions over orbital motions, then we have an understandable picture. In 2007, we see excess emission on the blue side of the $H\beta$ profile and the longest time lags indicating inflow (Denney et al. 2010). In 2012, we see the peak emission shifted redward to near zero velocities, and larger time lags near zero and

slightly redshifted velocities, indicating some dynamics more similar to outflow (De Rosa et al. 2018). In 2019–2020, after an extended low state, we again see $H\beta$ time lags longest on the blue side as well excess emission on blue side, indicating inflow again (e.g. see also, Feng et al. (2021b)). In an object like NGC 3516 with a likely edge-on BLR dominated by radial flow as demonstrated by RM, the $H\beta$ profile asymmetries track the velocity-resolved time lag distributions. In some sense, we can perhaps regard this object’s BLR as now understood, and we can model it in the future.

There are several physical processes which are considered as a possible reason for such dramatic changes of the luminosity in outburst and changing the Seyfert type: variable absorption along the line of sight, various types of instabilities in the accretion disk, and tidal destruction of stars (TDE). The strong UV flux following the change can sublimate the dust in a biconical hollow outflow (see Oknyansky et al. 2015) and, as a result, we may see the BLR without obscuration. So, in some not-too-long time after the outburst the dust can reform and the object will be seen as a type 2 again, the broad lines hidden from our line of sight. The most significant problem concerning TDEs is too low of a cadence of such accidents, which cannot explain the amount of observed CL events. An alternative idea involving the tidal stripping of stars (Campana et al. 2015; Ivanov & Chernyakova 2006) could lead to more frequent (than TDEs) and recurrent events of dramatic changes in the AGN accretion rate. Recurrent CL events in AGN can find a natural explanation, as in models with instability in the AD as well as in the model with tidal stripping of stars. Recently Wang & Bon (2020) also suggested a novel explanation for CL events, and for their recurrences in individual objects, by invoking the case of close binary black holes with a low mass ratio. For the last two models, an asymmetrical distribution of gas clouds near the AD may be expected.

Our observations of NGC 3516 during this latest CL event will not solve the problem of CL events more generally, but they do add to the phenomenology that must be addressed by proposed explanations. More references on the topic can be found in discussions by MacLeod et al. (2019); Oknyansky et al. (2017, 2019c); Runnoe et al. (2016); Ruan et al. (2019).

ACKNOWLEDGEMENTS

P. Du acknowledges financial support from the National Science Foundation of China (12022301, 11873048 and 11991051) and from the Strategic Priority Research Program of the CAS (XDB23010400). J.-M. Wang acknowledges financial support from the National Science Foundation of China (11991054 and 11833008), from the National Key R&D Program of China (2016YFA0400701), from the Key Research Program of Frontier Sciences of the Chinese Academy of Sciences (CAS; QYZDJ-SSW-SLH007), and from the CAS Key Research Program (KJZD-EW-M06).

Part of this work was supported by the M.V. Lomonosov Moscow State University Program of Development (RC600 & TDS). EOM, SAP, NIS, AVD acknowledge the support by the Interdisciplinary Scientific and Educational School of Moscow University ‘Fundamental and Applied Space Research’. EOM, NIS, AVD, AMT, SGJ are also supported by the RSF grant 17-12-01241. We thank the *Swift* team for carrying out our ToO requests. We are grateful to R. Oknyansky for help with ICCF and JAVELIN code installation and adoption. We thank WIRO engineers James Weger and J. Conrad Vogel for their observatory support. This work is supported by the National Science Foundation under REU grant

AST1852289 and PAARE grant AST 1559559. Michael Brotherton enjoyed support from the Chinese Academy of Sciences President’s International Fellowship Initiative, Grant No. 2018VMA0005. We also acknowledge support from a University of Wyoming Science Initiative Faculty Innovation Seed Grant. T.E. Zastrocky acknowledges support from NSF Grant 1003588R.

DATA AVAILABILITY

The data underlying this article are available in the article and in its online supplementary material.

REFERENCES

- Andrillat Y., Souffrin S., 1968, *Astrophys. Lett.*, **1**, 111
- Arnaud K. A., 1996, in Jacoby G. H., Barnes J., eds, *Astronomical Society of the Pacific Conference Series Vol. 101, Astronomical Data Analysis Software and Systems V*. p. 17
- Berdnikov L. N., Belinski A. A., Shatsky N. I., Burlak M. A., Ikonnikova N. P., Mishin E. O., Cheryasov D. V., Zhuyko S. V., 2020, *Astronomy Reports*, **64**, 310
- Buisson D. J. K., Lohfink A. M., Alston W. N., Fabian A. C., 2017, *MNRAS*, **464**, 3194
- Burrows D. N., et al., 2005, *Space Sci. Rev.*, **120**, 165
- Cackett E. M., Horne K., Winkler H., 2007, *MNRAS*, **380**, 669
- Campana S., Mainetti D., Colpi M., Lodato G., D’Avanzo P., Evans P. A., Moretti A., 2015, *A&A*, **581**, A17
- Cherepashchuk A. M., Lyutyi V. M., 1973, *Astrophys. Lett.*, **13**, 165
- Dalla Bontà E., et al., 2020, *ApJ*, **903**, 112
- De Rosa G., et al., 2018, *ApJ*, **866**, 133
- Denney K. D., et al., 2009, *ApJ*, **704**, L80
- Denney K. D., et al., 2010, *ApJ*, **721**, 715
- Dibai É. A., Pronik V. I., 1968, *Soviet Ast.*, **11**, 767
- Done C., Gierliński M., Kubota A., 2007, *A&ARv*, **15**, 1
- Du P., et al., 2014, *ApJ*, **782**, 45
- Du P., et al., 2018, *ApJ*, **869**, 142
- Edelson R., et al., 2017, *ApJ*, **840**, 41
- Evans P. A., et al., 2009, *MNRAS*, **397**, 1177
- Fausnaugh M. M., et al., 2016, *ApJ*, **821**, 56
- Feng H.-C., et al., 2021a, arXiv e-prints, p. arXiv:2103.03508
- Feng H.-C., et al., 2021b, *ApJ*, **909**, 18
- Fitch W. S., Pacholczyk A. G., Weymann R. J., 1967, *ApJ*, **150**, L67
- Gardner E., Done C., 2017, *MNRAS*, **470**, 3591
- Gaskell C. M., Sparke L. S., 1986, *ApJ*, **305**, 175
- Gehrels N., et al., 2004, *ApJ*, **611**, 1005
- Goad M. R., et al., 2019, *MNRAS*, **486**, 5362
- Grier C. J., et al., 2012, *ApJ*, **744**, L4
- Grier C. J., et al., 2013, *ApJ*, **764**, 47
- HI4PI Collaboration et al., 2016, *A&A*, **594**, A116
- Ilić D., et al., 2020, *A&A*, **638**, A13
- Ivanov P. B., Chernyakova M. A., 2006, *A&A*, **448**, 843
- Iwasawa K., Miniutti G., Fabian A. C., 2004, *MNRAS*, **355**, 1073
- Korista K. T., Goad M. R., 2001, *ApJ*, **553**, 695
- Koshida S., et al., 2014, *ApJ*, **788**, 159
- Kovačević A. B., Popović L. Č., Ilić D., 2020, *Open Astronomy*, **29**, 51
- Li I-Hsiu J., et al., 2019, *ApJ*, **884**, 119
- Lira P., Arévalo P., Uttley P., McHardy I. M. M., Videla L., 2015, *MNRAS*, **454**, 368
- Lyutyi V. M., Doroshenko V. T., 1993, *Astronomy Letters*, **19**, 405
- MacLeod C. L., et al., 2016, *MNRAS*, **457**, 389
- MacLeod C. L., et al., 2019, *ApJ*, **874**, 8
- Maoz D., Markowitz A., Edelson R., Nandra K., 2002, *AJ*, **124**, 1988
- McHardy I. M., et al., 2014, *MNRAS*, **444**, 1469
- Morgan C. W., Kochanek C. S., Morgan N. D., Falco E. E., 2010, *ApJ*, **712**, 1129

- Noda H., et al., 2016, *ApJ*, **828**, 78
- Oknyanskii V. L., 1993, *Astron. Lett.*, **19**, 416
- Oknyansky V. L., Gaskell C. M., Shimanovskaya E. V., 2015, *Odessa Astronomical Publications*, **28**, 175
- Oknyansky V. L., et al., 2017, *MNRAS*, **467**, 1496
- Oknyansky V. L., Winkler H., Tsygankov S. S., Lipunov V. M., Gorbovskoy E. S., van Wyk F., Buckley D. A. H., Tyurina N. V., 2019a, *Odessa Astronomical Publications*, **32**, 75
- Oknyansky V. L., Shenavrin V. I., Metlova N. V., Gaskell C. M., 2019b, *Astronomy Letters*, **45**, 197
- Oknyansky V. L., Winkler H., Tsygankov S. S., Lipunov V. M., Gorbovskoy E. S., van Wyk F., Buckley D. A. H., Tyurina N. V., 2019c, *MNRAS*, **483**, 558
- Oknyansky V. L., Mikailov K. M., Huseynov N. A., 2020a, *Astronomy Reports*, **64**, 979
- Oknyansky V. L., et al., 2020b, *MNRAS*, **498**, 718
- Oknyansky V. L., et al., 2020c, *The Astronomer's Telegram*, **13691**, 1
- Pancoast A., Brewer B. J., Treu T., Park D., Barth A. J., Bentz M. C., Woo J.-H., 2014, *MNRAS*, **445**, 3073
- Peterson B. M., 2004, in Storch-Bergmann T., Ho L. C., Schmitt H. R., eds, *IAU Symposium Vol. 222, The Interplay Among Black Holes, Stars and ISM in Galactic Nuclei*. pp 15–20 ([arXiv:astro-ph/0404539](https://arxiv.org/abs/astro-ph/0404539)), [doi:10.1017/S1743921304001358](https://doi.org/10.1017/S1743921304001358)
- Peterson B. M., Wanders I., Horne K., Collier S., Alexander T., Kaspi S., Maoz D., 1998, *PASP*, **110**, 660
- Peterson B. M., et al., 2014, *ApJ*, **795**, 149
- Potinin S. A., et al., 2020, *Astronomy Letters*, **46**, 836
- Risaliti G., Young M., Elvis M., 2009, *ApJ*, **700**, L6
- Ruan J. J., Anderson S. F., Eracleous M., Green P. J., Haggard D., MacLeod C. L., Runnoe J. C., Sobolewska M. A., 2019, *ApJ*, **883**, 76
- Runco J. N., et al., 2016, *ApJ*, **821**, 33
- Runnoe J. C., et al., 2016, *MNRAS*, **455**, 1691
- Seyfert C. K., 1943, *ApJ*, **97**, 28
- Shapovalova A. I., et al., 2019, *MNRAS*, **485**, 4790
- Shappee B. J., et al., 2014, *ApJ*, **788**, 48
- Strateva I. V., et al., 2003, *AJ*, **126**, 1720
- Sun M., Grier C. J., Peterson B. M., 2018, *PyCCF: Python Cross Correlation Function for reverberation mapping studies* (ascl:1805.032)
- Turner T. J., Miller L., Kraemer S. B., Reeves J. N., 2011, *ApJ*, **733**, 48
- Wachter K., Leach R., Kellogg E., 1979, *ApJ*, **230**, 274
- Wanders I., et al., 1993, *A&A*, **269**, 39
- Wang J.-M., Bon E., 2020, *arXiv e-prints*, p. [arXiv:2010.04417](https://arxiv.org/abs/2010.04417)
- Woo J.-H., Yoon Y., Park S., Park D., Kim S. C., 2015, *ApJ*, **801**, 38
- Zetzl M., et al., 2018, *A&A*, **618**, A83
- Zu Y., Kochanek C. S., Peterson B. M., 2011, *ApJ*, **735**, 80
- Zu Y., Kochanek C. S., Kozłowski S., Udalski A., 2013, *ApJ*, **765**, 106

This paper has been typeset from a $\text{\TeX}/\text{\LaTeX}$ file prepared by the author.